Journal of the Meteorological Society of Japan

EARLY ONLINE RELEASE

This is a PDF of a manuscript that has been peer-reviewed and accepted for publication. As the article has not yet been formatted, copy edited or proofread, the final published version may be different from the early online release.

The DOI for this manuscript is
DOI:10.2151/jmsj.2022-043
J-STAGE Advance published date: July 7th, 2022
The final manuscript after publication will replace the preliminary version at the above DOI once it is available.

ASUCA: The JMA Operational Non-hydrostatic Model

ISHIDA Junichi

Numerical Prediction Division, Japan Meteorological Agency, Tokyo, Japan

ARANAMI Kohei

Office of Marine Prediction, Japan Meteorological Agency, Tokyo, Japan

KAWANO Kohei

Numerical Prediction Development Center, Japan Meteorological Agency, Tsukuba, Japan

MATSUBAYASHI Kengo

Numerical Prediction Development Center, Japan Meteorological Agency, Tsukuba, Japan

KITAMURA Yuji

Numerical Prediction Development Center, Japan Meteorological Agency, Tsukuba, Japan

MUROI Chiashi

Planning Division, Japan Meteorological Agency, Tokyo, Japan

June 27, 2022

Corresponding author: ISHIDA Junichi, Numerical Prediction Division, Japan Meteorological Agency, 3-6-9 Toranomon, Minato City, Tokyo, 105-8431, Japan. E-mail: j-ishida@met.kishou.go.jp

Abstract

The non-hydrostatic numerical weather prediction (NWP) model ASUCA developed by the Japan Meteorological Agency (JMA) was launched into operation as 2 and 5 km-resolution regional models in 2015 and 2017, respectively. This paper outlines specifications of ASUCA with focus on the dynamical core and its configuration/accuracy as an operational model. ASUCA is designed for high computational stability and efficiency, mass conservation and forecast accuracy. High computational stability is achieved via a time-split integration scheme to compute acoustic terms and an advection scheme with a flux-limiter function to avoid numerical oscillation. In addition, vertical advection and sedimentation are calculated together with another exclusive time-splitting technique. ASUCA adopts hybrid parallelization using Message Passing Interface (MPI) and Open Multi Processing (OpenMP) for high computational efficiency on massive parallel scalar computers. The three-dimensional arrays are allocated such that the vertical direction is the stride-one innermost dimension to make effective use of cache and multi-thread parallelization. This is particularly advantageous for physical processes evaluated in a vertical column. To ensure mass conservation, density rather than pressure is integrated as a prognostic variable in flux-form fully compressible governing equations. ASUCA exhibited better performance than the previous operational model in idealized and NWP

tests.

1. Introduction

Numerical weather prediction (NWP) models form the technical foundation of weather forecasting by the Japan Meteorological Agency (JMA); their precision directly affects the accuracy of weather advisories/warnings and various other types of weather information. As weather-related disasters in Japan have become more intensified in recent times, optimization of prediction accuracy is an important factor in disaster mitigation. Against such a background, stable operation and sustainable development of JMA's operational NWP model are vital.

JMA has operated regional mesoscale NWP models with 2 and 5 km horizontal resolutions since 2012 and 2006, respectively, for purposes including mitigation of disasters caused by torrential rain. The Agency began regional mesoscale NWP model operation in 2001 with a hydrostatic model featuring a horizontal resolution of 10 km. This was replaced in 2004 by the non-hydrostatic model JMA-NHM (Saito et al. 2001, 2006), which was initially developed for research and subsequently adopted for operational use.

Though the JMA-NHM had been utilized extensively in research fields, its operation highlighted various problems, such as difficulties in achieving numerical stability, high-performance computing and sophistication of an NWP system including data assimilation.

As the reliance on NWP products increases in weather forecasting, higher numerical stability is required. To improve the computational stability, various methods (including artificial horizontal diffusion) have been introduced to the JMA-NHM. However, the JMA-NHM has occasionally caused computational instability or produced artificial noise for various complex reasons. The strength of the artificial diffusions applied to avoid numerical instability have been set empirically due to a lack of any scientific basis for such determination. Furthermore, sedimentation and vertical advection for water substances are treated independently of each other in the JMA-NHM. This treatment often affects the vertical distribution of the water substances and numerical stability. Accordingly, the application of artificial numerical diffusions in the JMA-NHM does not solve this problem; an overall reconstruction of the dynamical core is required.

Another significant issue relates to the rapid progress of high-performance computing. JMA upgrades its supercomputer system every five or six years with an increased number of CPUs. The sixth-generation system (1996 – 2001) had only 4 CPU cores, while the seventh (2001 – 2006) and eighth (2006 - 2012) had 640 and 2,560 cores respectively. The number of CPUs in supercomputer systems is expected to maintain exponential growth, giving rise to an urgent need for higher parallel computation efficiency.

However, the various efforts implemented to solve these problems complicated the source code of the JMA-NHM, and eventually hindered further development toward higher forecast accuracy. To promote ongoing NWP model development, sophisticated code management was needed. Against this background, JMA began development of the new non-hydrostatic dynamical core ASUCA, which is a recursive acronym of “ASUCA is a System based on a Unified Concept for Atmosphere”, in 2007.

For high computational stability, the monotonicity-preserving advection scheme proposed by Koren(1993) is utilized to avoid numerical oscillation, and the third-order Runge-Kutta method (Wicker and Skamarock 2002) is employed. Time splitting is also applied for vertical advection and falling water substances to satisfy the Courant-Friedrichs-Lewy (CFL) condition. These enable the exclusion of additional terms for computational stability such as numerical diffusion and divergence damping (Skamarock and Klemp 1992). The terms for vertical advection and falling water substances are calculated together, as independent treatment may cause unrealistic vertical separation of water substances.

To ensure accurate mass conservation, density rather than pressure is integrated as a prognostic variable in flux-form fully compressible equations with the finite volume method. Horizontally split-explicit and vertically implicit time integration method based on the conservative Split-Explicit Time Integration Method (Klemp et al. 2007) is employed to control acoustic and gravity waves.

Hybrid parallelization using Message Passing Interface (MPI) and Open Multi Processing (OpenMP) is adopted for high computational efficiency on massive parallel scalar computers. Computation, communication and disk-I/O are overlapped as much as possible, and three-dimensional arrays are allocated such that the vertical is the stride-one innermost dimension to make effective use of cache, multi-thread parallelization and Single-Instruction Multi-Data (SIMD) instructions. This design enables ASUCA to achieve high scalability on current parallel supercomputer systems.

A modern software management system including source code review, documentation, version control and project management tools is used to improve code quality and ensure a scientific research basis. To promote the development of physical process schemes which play key roles on NWP performance, physical process schemes are implemented via an independent library of the ASUCA dynamical core. Here, physical process schemes are designed as vertical one-dimensional models with unified coding and interface rules to support development using single-column models. The data assimilation system (Ikuta et al. 2021) and the forecast model are managed with a unified source code tree to maintain consistency between the 4D-Var assimilation system and the forecast model. This system facilitates the development and maintenance of source code quality. Intensive testing and checking were performed in the development of the operational model to avoid unexpected effects such as downgraded forecast accuracy.

ASUCA was found to perform better than the JMA-NHM, and replaced it as the Local Forecast Model (LFM) with 2 km resolution in 2015 and as the Meso Scale Model (MSM) with 5 km resolution in 2017. The ASUCA-based Mesoscale Ensemble Prediction System (MEPS; Ono et al. 2021) and the 4D-Var assimilation system (Ikuta et al. 2021) have been operated to provide uncertainty information and initial fields for the MSM since 2019 and 2020, respectively.

This paper outlines specifications of ASUCA with focus on the dynamical core and its configuration/accuracy as an operational model. Section 2 details the governing equations, and Section 3 describes discretization including the treatment of advection and time integration along with the derivation of the split-explicit method. Parallelization, which is essential for future high performance computing (HPC), is detailed in Section 4, and Section 5 presents simple specifications of physical process schemes used in the operational system and their coupling with dynamics. Section 6 compares the performance of ASUCA to that of the JMA-NHM in idealized and realistic simulations, while Section 7 provides a summary and outlines the future development plan of ASUCA.

2. Governing Equations

ASUCA involves the use of non-hydrostatic fully compressible governing equations written in flux form for mass conservation. Spherical curvilinear orthogonal and hybrid terrain-following coordinates with a shallow assumption are employed. To enable application of Lambert conformal map projection (as supported by the JMA-NHM and used in operational regional NWPs), ASUCA employs generalized coordinates for flexible three-dimensional transformation. Map factors for conformal projection are incorporated into the transformation metric tensor. Derivation is described in JMA (2014).

ASUCA employs a total mass density ρ and a modified moist potential temperature θ_m, defined as

$$
\begin{aligned}
\rho &\equiv \rho_d + \rho_v + \rho_c + \rho_r + \rho_i + \rho_s + \rho_g, \\
\theta_m &\equiv \theta \left\{ 1 + \left(\frac{1-\epsilon}{\epsilon} \right) q_v - q_c - q_r - q_i - q_s - q_g \right\}.
\end{aligned}
\tag{1}
$$

The definition of θ_m is identical to that of Klemp et al.(2007) except in the incorporation of water substances. The subscripts d, v, c, r, i, s and g represent dry air, water vapor, cloud water, rain, cloud ice, snow and graupel, respectively. q_α is the ratio of the density of water substances α to the total mass density ($\alpha = v, c, r, i, s, g$). ϵ is the ratio of the gas constant for dry air R_d to the gas constant for water vapor R_v, and θ is the potential temperature defined as

$$\theta \equiv \frac{T}{\pi}. \tag{2}$$

π is the Exner function defined as

$$\pi = \left(\frac{p}{p_0}\right)^{\frac{R_d}{C_p}}, \tag{3}$$

where p is the total pressure of moist air, p_0 is the reference pressure (typically 10^5 Pascals), and C_p is approximated by the specific heat capacity of dry air at constant pressure.

The density ρ_b, which is the sum of dry air and water substances whose terminal fall velocity is assumed to be zero, is described as

$$\rho_b = \sum_{\alpha \neq \mathrm{sed}} \rho_\alpha = \rho \left(1 - \sum_{\alpha = \mathrm{sed}} q_\alpha\right), \tag{4}$$

where "sed" denote the collection of water substances which are assumed to have non-zero terminal velocity.

The Jacobian of transformation from the Cartesian coordinates (x, y, z) to generalized coordinates (ξ, η, ζ) is defined as

$$J \equiv \begin{vmatrix} \xi_x & \xi_y & \xi_z \\ \eta_x & \eta_y & \eta_z \\ \zeta_x & \zeta_y & \zeta_z \end{vmatrix}, \tag{5}$$

where, $\xi_x \equiv \frac{\partial \xi}{\partial x}\big|_{y,z}$ and the same description is applied to other metrics. A restriction is imposed on vertical coordinates to satisfy $\xi_z = \eta_z = 0$ as required for application of the split-explicit time integration scheme as seen in section 3.4.

Velocity components in generalized coordinates (U, V, W) are defined as

$$\begin{aligned} U &= \xi_x u + \xi_y v + \xi_z w \\ V &= \eta_x u + \eta_y v + \eta_z w \\ W &= \zeta_x u + \zeta_y v + \zeta_z w. \end{aligned} \tag{6}$$

Here, (u, v, w) represent velocity components in Cartesian coordinates. The terminal fall velocity of water substances α in generalized coordinates is defined as

$$W_{t\alpha} = \zeta_z w_{t\alpha}, \tag{7}$$

where $w_{t\alpha}$ is the terminal fall velocity in Cartesian coordinates.

The variables ρ, $\rho\theta_m$ and π are decomposed into the basic state and the related deviation as

$$\rho = \overline{\rho} + \rho', \quad \rho\theta_m = \overline{\rho\theta_m} + (\rho\theta_m)', \quad \pi = \overline{\pi} + \pi', \tag{8}$$

where the basic state is time-independent and satisfies the hydrostatic equilibrium

$$\gamma R_d \overline{\pi} \zeta_z \frac{\partial}{\partial \zeta} \left(\overline{\rho\theta_m} \right) + \overline{\rho} \mathfrak{g} = 0. \tag{9}$$

$\gamma = C_p/C_v$ is the ratio of the heat capacities, where C_v is the specific heat capacity of dry air at constant volume, and $\mathfrak{g}$ is gravity acceleration. The definitions of all variables are summarized in Appendix A.

2.1 Momentum equations

As described above, the basic equations are transformed to generalized coordinates using map projection with spherical curvilinear orthogonal coordinates based on a shallow assumption. The transformed equations of motion are described as

$$\frac{\partial}{\partial t}\left(\frac{1}{J}\rho u\right)+\frac{\partial}{\partial \xi}\left(\frac{1}{J}\rho u U\right)+\frac{\partial}{\partial \eta}\left(\frac{1}{J}\rho u V\right)+\frac{\partial}{\partial \zeta}\left(\frac{1}{J}\rho_b u W\right)$$
$$+\gamma R_d \pi\left\{\frac{1}{J}\xi_x\frac{\partial}{\partial \xi}(\rho\theta_m)'+\frac{1}{J}\eta_x\frac{\partial}{\partial \eta}(\rho\theta_m)'+\frac{1}{J}\zeta_x\frac{\partial}{\partial \zeta}(\rho\theta_m)'\right\} \tag{10}$$
$$=-\sum_{\alpha=\mathrm{sed}}\frac{\partial}{\partial \zeta}\left\{\frac{1}{J}\rho q_\alpha u\left(W+W_{t\alpha}\right)\right\}-\frac{1}{J}\rho v\Gamma-\frac{1}{J}\rho v f+\frac{1}{J}F_{\rho u},$$

$$\frac{\partial}{\partial t}\left(\frac{1}{J}\rho v\right)+\frac{\partial}{\partial \xi}\left(\frac{1}{J}\rho v U\right)+\frac{\partial}{\partial \eta}\left(\frac{1}{J}\rho v V\right)+\frac{\partial}{\partial \zeta}\left(\frac{1}{J}\rho_b v W\right)$$
$$+\gamma R_d \pi\left\{\frac{1}{J}\xi_y\frac{\partial}{\partial \xi}(\rho\theta_m)'+\frac{1}{J}\eta_y\frac{\partial}{\partial \eta}(\rho\theta_m)'+\frac{1}{J}\zeta_y\frac{\partial}{\partial \zeta}(\rho\theta_m)'\right\} \tag{11}$$
$$=-\sum_{\alpha=\mathrm{sed}}\frac{\partial}{\partial \zeta}\left\{\frac{1}{J}\rho q_\alpha v\left(W+W_{t\alpha}\right)\right\}+\frac{1}{J}\rho u\Gamma+\frac{1}{J}\rho u f+\frac{1}{J}F_{\rho v},$$

$$\frac{\partial}{\partial t}\left(\frac{1}{J}\rho w\right)+\frac{\partial}{\partial \xi}\left(\frac{1}{J}\rho w U\right)+\frac{\partial}{\partial \eta}\left(\frac{1}{J}\rho w V\right)+\frac{\partial}{\partial \zeta}\left(\frac{1}{J}\rho_b w W\right)$$
$$+\gamma R_d \pi\left\{\frac{1}{J}\zeta_z\frac{\partial}{\partial \zeta}(\rho\theta_m)'\right\}+\left(\frac{\rho'}{J}-\frac{\pi'}{\overline{\pi}}\frac{\overline{\rho}}{J}\right)\mathfrak{g} \tag{12}$$
$$=-\sum_{\alpha=\mathrm{sed}}\frac{\partial}{\partial \zeta}\left\{\frac{1}{J}\rho q_\alpha w\left(W+W_{t\alpha}\right)\right\}+\frac{1}{J}F_{\rho w},$$

where

$$\Gamma=u\frac{m_2}{m_1}\frac{\partial m_1}{\partial \eta}-v\frac{m_1}{m_2}\frac{\partial m_2}{\partial \xi}. \tag{13}$$

The variables m_1 and m_2 are map factors relating to map projections (Saito et al. 2001). f is the Coriolis parameter. $F_{\rho u}$, $F_{\rho v}$ and $F_{\rho w}$ are the source and sink terms of momentum based on physical processes for the x-, y-, and z-directions, respectively.

The governing equations are solved on the coordinate system based on hybrid terrain-following vertical coordinates and Lambert conformal projection in regional configurations, in which the metric tensor is determined by the vertical coordinate transformation factor and the map factors. Details of the map projection and vertical coordinates employed in the operational regional NWPs are given in Appendix B.

2.2 Equation for mass conservation

The equation for mass conservation is

$$\frac{\partial}{\partial t}\left(\frac{1}{J}\rho'\right)+\frac{\partial}{\partial \xi}\left(\frac{1}{J}\rho U\right)+\frac{\partial}{\partial \eta}\left(\frac{1}{J}\rho V\right)+\frac{\partial}{\partial \zeta}\left(\frac{1}{J}\rho_b W\right)=-\sum_{\alpha=\mathrm{sed}}\frac{\partial}{\partial \zeta}\left(\frac{1}{J}\rho q_\alpha\left(W+W_{t\alpha}\right)\right)+\frac{1}{J}F_\rho, \tag{14}$$

where F_ρ is the source, sink and sub-grid transport term of total mass density.

2.3 Prognostic equation for potential temperature

The thermodynamic equation is

$$\frac{\partial}{\partial t}\left(\frac{1}{J}\left(\rho\theta_m\right)'\right)+\frac{\partial}{\partial \xi}\left(\frac{1}{J}\rho\theta_m U\right)+\frac{\partial}{\partial \eta}\left(\frac{1}{J}\rho\theta_m V\right)+\frac{\partial}{\partial \zeta}\left(\frac{1}{J}\rho\theta_m W\right)=\frac{1}{J}\left(\rho_d+\frac{\rho_v}{\epsilon}\right)Q_\theta, \tag{15}$$

where Q_θ is diabatic heating.

2.4 Prognostic equation for water substances

The prognostic equation for the density of water substances is

$$\frac{\partial}{\partial t}\left(\frac{1}{J}\rho q_\alpha\right)+\frac{\partial}{\partial \xi}\left(\frac{1}{J}\rho q_\alpha U\right)+\frac{\partial}{\partial \eta}\left(\frac{1}{J}\rho q_\alpha V\right)+\frac{\partial}{\partial \zeta}\left(\frac{1}{J}\rho q_\alpha (W+W_{t_\alpha})\right)=\frac{1}{J}F_{\rho\alpha}, \tag{16}$$

where $F_{\rho\alpha}$ is the source and sink term for the density of water substances α based on physical processes.

2.5 State equation

Using ρ and θ_m, the state equation for the ideal gas can be written in the same manner as that for dry conditions:

$$p = R_d \pi \rho \theta_m. \tag{17}$$

3. Discretization

3.1 Spatial discretization

The grid structures of the model are the Arakawa-C type (Arakawa and Lamb 1977) in the horizontal direction and the Lorenz type (Lorenz 1960) in the vertical direction. The equations are spatially discretized using the finite volume method to conserve total mass across the entire domain; this mass is controlled by inflow and outflow from the lower and lateral boundaries.

3.2 Advection scheme

Numerical oscillation should be avoided because it can cause spurious negative values for positive definite prognostic variables (e.g. density) and computational instability. However, higher-order linear advection schemes except the first-order scheme are non-monotone (Godunov 1959). Accordingly, a flux limiter function combining the solutions of the higher-order scheme and the first-order scheme is used to achieve higher-order accuracy without spurious oscillations (Durran 2010). Here, let us consider a simple one-dimensional transport problem with a scalar variable ϕ,

$$\frac{\partial \phi}{\partial t} + \frac{\partial (u\phi)}{\partial x} = 0, \tag{18}$$

and discretize the advection term as

$$\begin{aligned} \mathcal{F}_{i+\frac{1}{2}} &= (u\phi)_{i+\frac{1}{2}} = \left[\phi_i + \frac{1}{2}\Phi(s_{i+\frac{1}{2}})\,(\phi_i - \phi_{i-1})\right] u_{i+\frac{1}{2}}, \\ s_{i+\frac{1}{2}} &= \frac{\phi_{i+1} - \phi_i}{\phi_i - \phi_{i-1}}, \end{aligned} \tag{19}$$

where $\mathcal{F}_{i+\frac{1}{2}}$, $u_{i+\frac{1}{2}}$, $s_{i+\frac{1}{2}}$ and $\Phi(s_{i+\frac{1}{2}})$ are the flux and wind speed at the edge of the i-th cell, the smoothness parameter and the flux limiter function, respectively.

The model employs the flux limiter function proposed by Koren(1993) which combines the third- and first-order upwind schemes using the smoothness parameter s:

$$\Phi(s) = \max\left[0, \min\left\{2s, \frac{1}{3} + \frac{2}{3}s, 2\right\}\right]. \tag{20}$$

Figure 1 shows the Sweby diagram (Sweby 1984) for the flux limiter function in Eq. (20). The striped area indicates the region in which $\Phi(s)$ must lie to preserve monotonicity. When the distribution of ϕ_i is smooth, the parameter s is close to unity and $\Phi(s) = \frac{1}{3} + \frac{2}{3}s$. Equation (19) provides the third-order upwind scheme. However, when ϕ_i has a local minimum or maximum, s is negative and $\Phi(s)$ is zero. The equation then gives the first-order scheme. Thus, the third-order upwind scheme, which provides high accuracy, and the first-order upwind scheme, which preserves monotonicity, are smoothly connected. Based on Eq. (20), Eq. (19) can be written as

$$\mathcal{F}_{i+\frac{1}{2}} = \begin{cases} \left[\phi_i + \max\left\{0, \min\left(x_i, y_i, z_i\right)\right\}\right] u_{i+\frac{1}{2}} & (x_i \geq 0) \\ \left[\phi_i + \min\left\{0, \max\left(x_i, y_i, z_i\right)\right\}\right] u_{i+\frac{1}{2}} & (x_i < 0) \end{cases} \tag{21}$$

$$x_i = \phi_i - \phi_{i-1}, \quad y_i = \phi_{i+1} - \phi_i, \quad z_i = \frac{x_i}{6} + \frac{y_i}{3}.$$

Note that division by zero disappears in Eq. (21) in contrast to Eq. (20).

Figure 2 shows the results of a one-dimensional (1D) transport problem in comparison with the first- and third-order advection schemes. A rectangular pulse is advected 2500 time steps in a 200 grid periodic domain using Courant number of 0.16. In the test, the time integration scheme in Section 3.3 is used. It can be seen that Koren's flux limiter suppresses overshoot and undershoot without numerical diffusions. Fig. 1

Fig. 2

3.3 *Time integration*

The three-stage third-order Runge-Kutta (RK3) scheme proposed by Wicker and Skamarock(2002) is adopted for time integration. In this scheme, the differential equation

$$\frac{d\phi}{dt} = F(\phi), \tag{22}$$

is integrated from $\phi(t)$ to $\phi(t + \Delta t)$ as

$$\phi^* = \phi(t) + F(\phi(t)) \cdot \frac{1}{3}\Delta t,$$

$$\phi^{**} = \phi(t) + F(\phi^*) \cdot \frac{1}{2}\Delta t,$$

$$\phi(t+\Delta t) = \phi(t) + F(\phi^{**}) \cdot \Delta t.$$

This helps to reduce memory consumption because the updated value in each stage can be calculated from the value in the previous stage and $\phi(t)$.

3.4 Horizontally explicit and vertically implicit (HE-VI) scheme

Terms related to sound waves and gravity waves are evaluated on a short time step using a horizontally explicit and vertically implicit (HE-VI) scheme (Klemp et al. 2007) and the RK3 scheme is also applied on the short time step. Forward time integrations with the short time step $\Delta\tau$ are used for the horizontal momentum equations:

$$\left(\frac{1}{J}\rho u\right)^{\tau+\Delta\tau} = \left(\frac{1}{J}\rho u\right)^{\tau} - \gamma R_d \pi^t \left\{\frac{1}{J}\xi_x\frac{\partial}{\partial\xi}(\rho\theta_m)'^{\tau} + \frac{1}{J}\eta_x\frac{\partial}{\partial\eta}(\rho\theta_m)'^{\tau} + \frac{1}{J}\zeta_x\frac{\partial}{\partial\zeta}(\rho\theta_m)'^{\tau}\right\}\Delta\tau + \mathfrak{R}_u^t\Delta\tau, \tag{23}$$

$$\left(\frac{1}{J}\rho v\right)^{\tau+\Delta\tau} = \left(\frac{1}{J}\rho v\right)^{\tau} - \gamma R_d \pi^t \left\{\frac{1}{J}\xi_y\frac{\partial}{\partial\xi}(\rho\theta_m)'^{\tau} + \frac{1}{J}\eta_y\frac{\partial}{\partial\eta}(\rho\theta_m)'^{\tau} + \frac{1}{J}\zeta_y\frac{\partial}{\partial\zeta}(\rho\theta_m)'^{\tau}\right\}\Delta\tau + \mathfrak{R}_v^t\Delta\tau, \tag{24}$$

where

$$
\begin{aligned}
\mathfrak{R}_u = & -\frac{\partial}{\partial \xi}\left(\frac{1}{J}\rho u U\right) - \frac{\partial}{\partial \eta}\left(\frac{1}{J}\rho u V\right) - \frac{\partial}{\partial \zeta}\left(\frac{1}{J}\rho u W\right) \\
& -\sum_{\alpha} \frac{\partial}{\partial \zeta}\left(\frac{1}{J}\rho u q_\alpha W_{t_\alpha}\right) - \frac{1}{J}\rho v \Gamma - \frac{1}{J}\rho v f + \frac{1}{J}F_{\rho u},
\end{aligned} \tag{25}
$$

$$
\begin{aligned}
\mathfrak{R}_v = & -\frac{\partial}{\partial \xi}\left(\frac{1}{J}\rho v U\right) - \frac{\partial}{\partial \eta}\left(\frac{1}{J}\rho v V\right) - \frac{\partial}{\partial \zeta}\left(\frac{1}{J}\rho v W\right) \\
& -\sum_{\alpha} \frac{\partial}{\partial \zeta}\left(\frac{1}{J}\rho v q_\alpha W_{t_\alpha}\right) + \frac{1}{J}\rho u \Gamma + \frac{1}{J}\rho u f + \frac{1}{J}F_{\rho v}.
\end{aligned} \tag{26}
$$

The pressure gradient / buoyancy terms in the vertical momentum equation and the vertical advection terms in the potential temperature / density equations are implicitly evaluated to ensure computational stability as

$$
\left(\frac{1}{J}\rho w\right)^{\tau+\Delta\tau} = \left(\frac{1}{J}\rho w\right)^{\tau} - \left\{\gamma R_d {\pi^t} \frac{1}{J}\zeta_z \frac{\partial}{\partial \zeta}(\rho\theta_m)'^{\tau+\Delta\tau} + \frac{\rho'^{\tau+\Delta\tau}}{J}\mathfrak{g} - \frac{\pi'^t}{\overline{\pi}}\frac{\overline{\rho}}{J}\mathfrak{g}\right\}\Delta\tau + \mathfrak{R}_w^t \Delta\tau, \tag{27}
$$

$$
\left(\frac{1}{J}(\rho\theta_m)'\right)^{\tau+\Delta\tau} = \left(\frac{1}{J}(\rho\theta_m)'\right)^{\tau} - \left\{\frac{\partial}{\partial \zeta}\left(\frac{1}{J}\zeta_z \theta_m^\tau (\rho w)^{\tau+\Delta\tau}\right)\right\}\Delta\tau + \mathfrak{R}_{\theta_m}^t \Delta\tau, \tag{28}
$$

$$
\left(\frac{1}{J}\rho'\right)^{\tau+\Delta\tau} = \left(\frac{1}{J}\rho'\right)^{\tau} - \left\{\frac{\partial}{\partial \zeta}\left(\frac{1}{J}\zeta_z (\rho w)^{\tau+\Delta\tau}\right)\right\}\Delta\tau + \mathfrak{R}_{\rho}^t \Delta\tau, \tag{29}
$$

where

$$
\begin{aligned}
\mathfrak{R}_w =& -\frac{\partial}{\partial \xi}\left(\frac{1}{J}\rho w U\right) - \frac{\partial}{\partial \eta}\left(\frac{1}{J}\rho w V\right) - \frac{\partial}{\partial \zeta}\left(\frac{1}{J}\rho w W\right) \\
& - \sum_{\alpha} \frac{\partial}{\partial \zeta}\left(\frac{1}{J}\rho w q_\alpha W_{t_\alpha}\right) + \frac{1}{J}F_{\rho w}, \\
\mathfrak{R}_{\theta_m} =& -\left\{\frac{\partial}{\partial \xi}\left(\frac{1}{J}\theta_m \widetilde{(\rho U)}\right) + \frac{\partial}{\partial \eta}\left(\frac{1}{J}\theta_m \widetilde{(\rho V)}\right) + \frac{\partial}{\partial \zeta}\left(\frac{1}{J}\theta_m \widetilde{(\rho W)}\right)\right\} \\
& + \frac{1}{J}\left(\rho_d + \frac{\rho_v}{\epsilon}\right) Q_\theta, \\
\mathfrak{R}_{\rho} =& -\left\{\frac{\partial}{\partial \xi}\left(\frac{1}{J}\widetilde{(\rho U)}\right) + \frac{\partial}{\partial \eta}\left(\frac{1}{J}\widetilde{(\rho V)}\right) + \frac{\partial}{\partial \zeta}\left(\frac{1}{J}\widetilde{(\rho W)}\right)\right\} \\
& - \sum_{\alpha} \frac{\partial}{\partial \zeta}\left(\frac{1}{J}\rho q_\alpha W_{t_\alpha}\right) + \frac{1}{J}F_{\rho},
\end{aligned}
\tag{30}
$$

and

$$\widetilde{(\rho U)} = \xi_x (\rho u)^{\tau+\Delta\tau} + \xi_y (\rho v)^{\tau+\Delta\tau}, \tag{31}$$

$$\widetilde{(\rho V)} = \eta_x (\rho u)^{\tau+\Delta\tau} + \eta_y (\rho v)^{\tau+\Delta\tau}, \tag{32}$$

$$\widetilde{(\rho W)} = \zeta_x (\rho u)^{\tau+\Delta\tau} + \zeta_y (\rho v)^{\tau+\Delta\tau}. \tag{33}$$

It should be noted that terms including $(\rho w)^{\tau+\Delta\tau}$ in Eqs (31) – (33) are omitted under the assumption that the vertical coordinate is restricted to satisfy $\xi_z = \eta_z = 0$ as outlined in Section 2. This restriction is necessary for the vertical implicit treatment of Eqs (27) – (29). Eliminating $\left(\frac{1}{J}(\rho\theta_m)'\right)^{\tau+\Delta\tau}$ and $\left(\frac{1}{J}\rho'\right)^{\tau+\Delta\tau}$ from Eq. (27) using Eqs (28) and (29), the one dimensional Helmholtz type equation for $\omega \equiv \left(\frac{1}{J}\rho w\right)^{\tau+\Delta\tau}$ is determined as

$$-\Delta\tau^2\gamma R_d\pi^t\frac{1}{J}\zeta_z\frac{\partial}{\partial\zeta}\left(J\frac{\partial}{\partial\zeta}\left(\zeta_z\theta_m^\tau\omega\right)\right)-\Delta\tau^2\mathfrak{g}\frac{\partial}{\partial\zeta}\left(\zeta_z\omega\right)+\omega=\mathfrak{R}, \tag{34}$$

where

$$\begin{aligned}\mathfrak{R}=&\left(\frac{1}{J}\rho w\right)^\tau-\gamma R_d\pi^t\Delta\tau\frac{1}{J}\zeta_z\frac{\partial}{\partial\zeta}\left\{(\rho\theta_m)'^\tau+J\mathfrak{R}_{\theta_m}\Delta\tau\right\}\\&-\Delta\tau\mathfrak{g}\left(\frac{1}{J}\rho'^\tau+\mathfrak{R}_\rho\Delta\tau\right)+\left\{-\left(1-\frac{\pi^t}{\overline{\pi}}\right)\frac{\overline{\rho}}{J}\mathfrak{g}+\mathfrak{R}_w\right\}\Delta\tau.\end{aligned} \tag{35}$$

$\omega=0$ is imposed at the top and bottom boundaries upon resolution of the Helmholtz equation. This is derived from $W=0$ at these boundaries.

3.5 Time splitting

a. Time splitting for vertical advection

For real-case simulations including physical processes, a strong vertical velocity that does not satisfy the CFL condition is often computed. To ensure computational stability, ASUCA employs a time-splitting scheme for evaluation of vertical advection on the basis of the three-dimensional CFL condition.

The stability condition of three-dimensional advection depends on the advection scheme as well as the time integration scheme. The CFL condition for the advection and time integration schemes used in ASUCA is given as,

$$
\begin{aligned}
C_1 &\leq C_{\mathrm{crit}}, \\
C_{\mathrm{crit}} &\simeq 1.25,
\end{aligned}
\tag{36}
$$

where, C_1 is the Courant number for 1D advection and C_{crit} is the critical value for satisfying the CFL condition as is shown in Appendix C. As described in Section 3.3, the RK3 scheme is employed in ASUCA with parallel splitting (Dubal et al. 2004) of advection in each direction. The CFL condition for these specifications is

$$
C_\xi + C_\eta + C_\zeta \leq C_{\mathrm{crit}}, \tag{37}
$$

where C_ξ, C_η and C_ζ are the Courant numbers in the ξ, η and ζ directions, respectively. As this condition can be easily violated in typhoons with stormy horizontal winds and strong updrafts, time splitting for vertical advection is adopted. When a time step in evaluation of vertical advection (in the ζ direction) is divided into N substeps, the condition of Eq. (37) is modified to

$$
C_\xi + C_\eta + C_\zeta/N \leq C_{\mathrm{crit}}. \tag{38}
$$

In the model, time splitting is applied to columns where

$$C_\xi + C_\eta + C_\zeta \geq \lambda C_{\text{crit}}. \tag{39}$$

Here, λ is a safety coefficient set as 0.95 in ASUCA.

When time splitting is invoked, RK3 for the short time step $\Delta\tau$ is nested in the original RK3 time integration with the time step Δt (Fig. 3). Note that $\Delta\tau$ is given independent of the short time step for the HE-VI scheme described in Section 3.4. This involves greater computational cost, but produces the desired higher stability. Divergence damping can be excluded using RK3 for short time steps. This is desirable for accurate dispersion relations in compressible equations (e.g. Gassmann and Herzog 2007). Fig. 3

In time splitting, horizontal and vertical advection are evaluated sequentially (Dubal et al. 2004). The prognostic variables are updated using the horizontal flux $\mathcal{F}_\xi$ and $\mathcal{F}_\eta$, and vertical flux $\mathcal{F}_\zeta$ is then evaluated with the updated variables as

$$\phi^{H*} = \phi^n - \left(\frac{\partial}{\partial \xi} {\mathcal{F}_\xi}^n + \frac{\partial}{\partial \eta} {\mathcal{F}_\eta}^n \right) \Delta\tau, \tag{40}$$

$$\phi^{n+1} = \phi^{H*} - \left(\frac{\partial}{\partial \zeta} {\mathcal{F}_\zeta}^{H*} \right) \Delta\tau. \tag{41}$$

Sequential time splitting is advantageous for its higher computational stability as compared to parallel splitting. However, this approach produces directional distortion because the updated value ϕ^{n+1} depends on the evaluation sequence. Accordingly, sequential splitting is used only when the condition of Eq. (37) cannot be satisfied in order to minimize errors.

b. Time splitting for sedimentation of precipitable water substances

As sedimentation of precipitable water substances (e.g., rain, snow and graupel) with high terminal velocity can cause computational instability, a time-splitting method is employed. The vertical velocities of such substances are defined as the sum of the vertical velocity of air W and the terminal velocities $W_{t\alpha}$ as determined from cloud microphysics (e.g. Gunn and Kinzer 1949).

The time-split interval $\Delta\tau_{\rm sed}$ for sedimentation is dynamically determined for each column depending on the Courant number $C_{\rm sed}$ for sedimentation. This number for the first time-split step at the vertical level k of the column is defined as

$$C^1_{{\rm sed},k} = \frac{(W^1_k + W^1_{t\alpha,k})\Delta t}{\Delta\zeta_k}, \tag{42}$$

where the overscript 1 indicates the first time-level index of the time-split step.

The first time-split step interval $\Delta\tau^1_{\rm sed}$ for the column is then determined as

$$\Delta\tau_{\rm sed}^1 = \begin{cases} \Delta t & (\max(C_{{\rm sed},k}^1) \le 1) \\ \beta \dfrac{\Delta t}{\max(C_{{\rm sed},k}^1)} & (\max(C_{{\rm sed},k}^1) > 1). \end{cases} \tag{43}$$

Here, $\max(C_{{\rm sed},k}^1)$ is the maximum Courant number for the column and β is a parameter for determining time-split step set as 0.9 in ASUCA.

After time integration with $\Delta\tau_{\rm sed}^1$, the residual time step is $\Delta t' = \Delta t - \Delta\tau_{\rm sed}^1$. The next time-split step interval $\Delta\tau_{\rm sed}^2$ is determined from the Courant number $C_{{\rm sed},k}^2 = (W_k^2 + W_{t\alpha,k}^2)\Delta t'/\Delta\zeta_k$ using the updated terminal velocities $W_{t\alpha,k}^2$, and time integration with $\Delta\tau_{\rm sed}^2$ is calculated. This procedure is repeated until no residual time step is left.

3.6 Boundary conditions

a. Rayleigh damping

To prevent wave reflection at the lateral and upper boundaries, the Rayleigh damping term

$$\frac{\partial\phi}{\partial t} = -m\,(x,y,z)\,[\phi(t) - \phi_{\rm ext}(t)]\,, \tag{44}$$

is added to the time tendencies of the prognostic variables ρ', ρu, ρv, ρw,$(\rho\theta_m)'$ and ρq_α near the boundaries. In Eq. (44), ϕ denotes the prognostic variable at the first state of each time step (i.e., Eq. (44) is solved explicitly), and ϕ_{ext} is the value of the parent model providing the lateral and upper boundaries in regional configurations. As the parent model provides the boundary data with a much larger time interval and coarser resolution than that of the model, ϕ_{ext} is interpolated in time and space from the provided data. It should be noted that $\rho w_{\text{ext}} = 0$.

The location-based function $m\,(x, y, z)$ is used to determine the 1/e-folding time for the boundaries. The function has a maximum at the boundary and decreases with subsequent grid point distance defined as

$$m(x, y, z) = \max(m_x, m_y, m_z), \tag{45}$$

where

$$m_x = \begin{cases} \gamma_h \sin^2\left[\frac{\pi}{2}\left(1 - \frac{d_x}{d_h}\right)\right] & (d_x < d_h) \\ 0 & (d_x \geq d_h), \end{cases} \tag{46}$$

$$m_y = \begin{cases} \gamma_h \sin^2\left[\frac{\pi}{2}\left(1 - \frac{d_y}{d_h}\right)\right] & (d_y < d_h) \\ 0 & (d_y \geq d_h), \end{cases} \tag{47}$$

$$m_z = \begin{cases} \gamma_v \sin^2\left[\frac{\pi}{2}\left(1 - \frac{d_z}{d_v}\right)\right] & (d_z < d_v) \\ 0 & (d_z \geq d_v). \end{cases} \tag{48}$$

Here, d_x, d_y and d_z are the distances from the boundaries, d_h and d_v are the distances from the lateral and upper boundaries where Rayleigh damping is observed, and γ_h and γ_v are parameters determining damping strength, respectively. d_h, d_v, γ_h and γ_v are empirically determined.

b. *Lateral flux adjustment*

In regional models, changes in total mass depend on i) the source and sink terms at the surface (i.e. evaporation and precipitation), ii) the density change due to Rayleigh damping, and iii) inflow and outflow at the upper and lateral boundaries as determined from the parent model covering the regional model's domain. As the orders of magnitude of i), ii) and iii) are 10^{11}, 10^{11} and 10^{13} [kg] respectively in the operational LFM, we assume i) and ii) are negligible in relation to iii). Then, the change in total mass can be approximated as

$$\frac{\partial M(t)}{\partial t} = F(t), \tag{49}$$

where $M(t)$ and $F(t)$ are the total mass in the model domain and the sum of mass flux at the boundaries, respectively. As the parent model provides $M(t)$ and $F(t)$ with a time interval much larger than that of the model, regional models must compute $F(t)$ at each time step by interpolating boundary data temporally. However, this produces an overall mass error because the interpolated mass flux $F_g(t)$ differs from the parent model prediction, i.e.:

$$M^p(t_{n+1}) - M^p(t_n) = \int_{t_n}^{t_{n+1}} F^p(t)dt \\ \neq \sum_{t=t_n}^{t_{n+1}} F_g(t)\Delta t. \tag{50}$$

Here, t_n and t_{n+1} are the times at which lateral boundary data are given, and the superscript p indicates variables predicted by the parent model. Note that $F_g(t)$ at each time step is computed by interpolating $F^p(t_n)$ and $F^p(t_{n+1})$ temporally and spatially. If the total mass flux predicted by the parent model $F^p(t)$ exceeds the interpolated mass flux $F_g(t)$, the regional model will predict a total mass smaller than this and, consequently, a lower pressure field. To reduce this error, correction for mass flux at boundaries is required in the regional model.

To ensure overall mass consistency with the parent model, regional configurations of ASUCA employ flux adjustment with the value $F_{adj}(t)$ modifying lateral inflow and outflow:

$$M^p(t_{n+1}) - M^p(t_n) = \sum_{t=t_n}^{t_{n+1}} \left[F_g(t) + F_{adj}(t)\right] \Delta t. \tag{51}$$

The adjustment does not correct mass flux at the upper boundary because vertical velocity at the model top is assumed to be zero (Section 3.4).

As there is no established approach for determining $F_g(t)$ and $F_{adj}(t)$ which satisfy Eq. (51), ASUCA employs a method that produces smooth $M(t)$ values with regard to time, and calculates $F_{adj}(t)$ consequently. $M(t)$ is approximated as a sequence of polynomials $M_n(t)$ via third-order spline interpolation as

$$M_n(t) \simeq a_n + b_n(t - t_n) + c_n(t - t_n)^2 + d_n(t - t_n)^3, \tag{52}$$

where $M_n(t_n) = M^p(t_n)$ and $M_n(t_{n+1}) = M^p(t_{n+1})$. a_n, b_n, c_n and d_n are coefficients in the interval $t_n \le t \le t_{n+1}$ and determined via spline interpolation (i.e., first and second derivatives of $M_n(t_n)$ is identical to $M_{n+1}(t_{n+1})$). Equations. (49) and (52) give $F(t)$ as

$$\begin{aligned} F(t) &= \frac{\partial M(t)}{\partial t}, \\ &= b_n + 2c_n(t - t_n) + 3d_n(t - t_n)^2. \end{aligned} \tag{53}$$

$F_g(t)$ is linearly interpolated using $F(t_n)$ and $F(t_{n+1})$, and $F_{adj}(t)$ is determined as

$$F_{adj}(t) = b_n + 2c_n(t - t_n) + 3d_n(t - t_n)^2 - F_g(t). \tag{54}$$

As ASUCA employs momentums for prognostic variables, horizontal momentum is adjusted to ensure mass consistency. To mitigate adjustment-related shock, horizontal momentum adjustment is applied over the whole domain rather than only at boundaries. The value is linearly reduced depending on distance from lateral boundaries as

$$
\begin{aligned}
\frac{1}{J}\rho\widehat{U}(t,\xi,\eta,\zeta) =& \frac{1}{J}\rho U(t,\xi,\eta,\zeta) + \left(1 - 2\frac{\mathrm{dx}(\xi)}{\mathrm{Dx}}\right) A(z,t) \\
\frac{1}{J}\rho\widehat{V}(t,\xi,\eta,\zeta) =& \frac{1}{J}\rho V(t,\xi,\eta,\zeta) + \left(1 - 2\frac{\mathrm{dy}(\eta)}{\mathrm{Dy}}\right) A(z,t),
\end{aligned}
\tag{55}
$$

where $\widehat{U}$ and $\widehat{V}$ are adjusted velocities. Dx and Dy are the sizes of the computational domain in the x- and y- directions, respectively, while $\mathrm{dx}(\xi)$ and $\mathrm{dy}(\eta)$ are the distances from the western and southern boundaries. $A(z,t)$ is the horizontal momentum adjustment defined as

$$
A(z,t) = \frac{F_{adj}(t)}{2(S_{\eta\zeta} + S_{\xi\zeta})} \frac{\overline{\rho}(z)\Delta z}{\int \overline{\rho}(z) dz}, \tag{56}
$$

where $S_{\eta\zeta}$ and $S_{\xi\zeta}$ are the areas of the sides of full model domain, $\overline{\rho}(z)$ is the basic state density, and $\frac{\overline{\rho}(z)\Delta z}{\int \overline{\rho}(z) dz}$ is the mass-fraction of the discretized grid in the vertical column. $A(z,t)$ is formulated so that total inflow at boundaries is equivalent to $F_{adj}(t)$ and adjustment horizontal velocity is approximately uniform with height.

This lateral flux adjustment enables ASUCA to predict total mass and pressure field values consistent with those of the parent model. Related performance is described in Section 6.2.

4. Parallel Computing

Parallel computing plays a crucial role in NWP modeling due to the current trend of supercomputer architecture toward massively parallel processing. To achieve high computational efficiency on massive parallel scalar computers, ASUCA employs hybrid parallelization using the OpenMP interface for shared memory parallelization and the MPI for distributed memory parallelization.

The three-dimensional arrays are allocated so that the vertical z is the stride-one innermost dimension to make the z- loop contiguous in the memory address, enabling ASUCA to make effective use of the CPU cache. This is also beneficial for code management, as physics schemes, which are generally designed as single-column models (Moncrieff et al. 1997), can be easily implemented in the model. Calculations of physical process schemes at different columns are essentially independent, meaning that OpenMP parallelization can be applied for horizontal loops.

The model domain is split into horizontally two-dimensional sub-domains, and each decomposed sub-domain is assigned to one of the MPI processes (Aranami and Ishida 2004). The OpenMP interface is used for parallelization inside the sub-domains. OpenMP threads are applied to loops for the y-direction, and in some horizontal loops, the x- and y-loops are fused to increase loop length such that load imbalance between threads is minimized.

The sub-domains have halo regions that are exchanged with immediately adjacent MPI processes. As MPI communication and file I/O are time-consuming operations with the current supercomputer architecture, two types of overlapping are used in the model to significantly improve computational efficiency. One is overlapping of halo exchanges with computation (Cats et al. 2008) to minimize the overhead of communication between MPI processes. The OpenMP interface is also used for this operation; while one thread calls a MPI function to exchange data in the halo region with another MPI process, the other threads simultaneously execute computation in the inner region. The other technique involves an I/O server approach to overlap file I/O with computation. Figure 4 illustrates a schematic diagram of the I/O server approach. In this method, certain MPI processes are dedicated to file I/O. While computation continues, dedicated I/O processes read data from disks and send them to the relevant computational processes. When output is required, the processes save the data in a dedicated buffer to invoke send operation and immediately continue computation. I/O processes receive the data and output them to the disk. In this approach, computation and disk I/O are asynchronously processed. It is advantageous for hiding disk I/O latency because disk I/O is a time consuming process. The optimum number of I/O ranks depends on calculation amount, frequency of disk I/O, and computer architecture. Fig. 4

Single-Instruction Multi-Data (SIMD) vectorization is applied to the innermost z- direction. However, this is not applicable for z-loops that have loop-carried dependency, such as the ordinary tri-diagonal matrix solver used in the vertical implicit solver for HE-VI (section 3.4), due to vertical dependency. To remedy the issue, the Ends Toward Center scheme (Samukawa 2001) is employed for better use of SIMD in the tri-diagonal matrix solver. This contributes to optimization of the model because this calculation is required at every short time step in the HE-VI scheme.

The parallel efficiency of ASUCA is shown in Fig.5 for the configuration of the operational LFM. In this experiment, a 10-hour forecast with 1,581 $\times$ 1,301 grid points in the horizontal and 58 layers in the vertical was produced with total input/output data sizes of 97 and 17 GB, respectively. Figure 5 shows the ideal and measured acceleration ratios from JMA's current supercomputer system Cray XC50 on which each of nodes is equipped with two Intel Xeon Platium 8160 processors with a clock frequency of 2.1GHz and 24 cores per processors (JMA 2019a). The horizontal axis represents the number of CPU cores. There are 8 OpenMP threads up to 14,400 cores while 12, 16 and 24 threads are used for 19,200 and 28,800, 24,000, and 38,400 and 48,000 cores, respectively. The model demonstrates more than 50% of ideal scalability up to 24,000 cores even though full-size output to the disk in operational LFM configuration is included in the elapsed time. Fig. 5

5. Physical Processes

Physical process schemes are implemented via the independent Physics Library of the ASUCA dynamical core (Hara et al. 2012). The library is a group of various subroutines related to physical process schemes, and provides a common interface based on the unified coding rules. Physical process schemes in the library are designed as the vertical one-dimensional models independently of the horizontal grids. This enables the constitution of a single-column model for unit testing and comparison of parameterization schemes. The coding policy is also suitable for modern scalar computers because an improved cache hit rate is crucial for processing speed.

The Physics Library is utilized in the procedures described here. Model variables are converted to variables required as arguments for subroutines implemented in the library. For instance, if the velocity u is required in the library, u is calculated from ρ and ρu which are the prognostic variables of ASUCA. The subroutine in the library calculates and returns the tendency of u, which is then converted to the tendency of the model variable ρu. Subroutines implemented in the library are not used to directly update prognostic variables. Hence, an NWP model can call a subroutine in a common style regardless of how it is implemented. These rules contribute to efficient updating of the physical process schemes applied to ASUCA. Table 1

The physical process schemes are regularly updated in operational use.

Those used in the LFM since March 2021 are summarized in Table 1, and the schemes are detailed in JMA (2019b). The surface scheme employs a tiled approach in which area fractions of different surface types such as land and sea are given in the same grid. Turbulent fluxes for all tiles are calculated, and a grid point value of these fluxes is evaluated as the weighted average in proportion to the area fraction of each tile in the grid.

Computational stability is essential for NWP model operation while a sufficiently small time step could not be adopted for evaluating physical processes, because calculation must finish within a certain time. To satisfy these contradictory requirements, some physical process schemes (e.g., cloud microphysics, surface flux and boundary layer) are implicitly calculated. In cloud microphysics, processes in which change rate of a variable is proportional to the amount of the variable itself (e.g., accretion of cloud ice by snow; Lin et al. 1983) are solved implicitly. It should be noted that vertical flux in the boundary layer scheme is evaluated independently of the surface flux scheme while both must be coupled for implicit evaluation. The Physics Library provides an implicit solver to enable coupling of the boundary layer and the surface schemes with these schemes implemented as separated packages.

In ASUCA, radiation, boundary layer and surface, and convection schemes are computed using the first state of time-steps independently of each other (i.e., parallel splitting; Dubal et al. 2004). Microphysics is computed at the end of time-steps sequentially to guarantee non-negative hydrometeors while saturation adjustment is computed at every RK3 steps.

6. Validation Tests for Operational Use

6.1 Ideal experiments

Various ideal experiments were conducted to validate basic ASUCA dynamics performance. Ishida et al.(2010) reported the results of experiments for non-hydrostatic inertia gravity waves as originally proposed by Skamarock and Klemp(1994), and for non-linear density current with the results obtained by Straka et al.(1993) referenced as a benchmark. The results of ideal mountain wave and rising thermal simulation tests are presented below in comparison with the JMA-NHM outcomes.

a. Mountain wave tests

ASUCA simulation provided better results than the JMA-NHM in a two-dimensional linear non-hydrostatic mountain wave test as per the "Standard Test Set for Non-hydrostatic Dynamical Cores of NWP Models" (Skamarock et al. 2004), which enables evaluation of simulated non-hydrostatic topographic flows based on comparison to the analytic solution.

Uniform flow with a constant wind speed of 10 ms^{-1} and a Brunt-Väisälä frequency of 0.01 s^{-1} over mountainous terrain were considered. The mountain profile, $h(x)$, was given as

$$h(x) = h/(1 + (x/a)^2), \tag{57}$$

where $a = 2$ km and $h = 1$ m. The computational domain size was 144 km horizontally and 30 km vertically, with the grid spacings of 400 and 250 m, respectively. The mountain is located at the center of the horizontal domain. Cyclic boundary conditions for the lateral boundaries were assumed, and Rayleigh damping was used for the top 6 km layers to relax the state back to the initial field to reduce the artificial reflection of gravity-wave. Time-step intervals of 3 and 1 s were used for ASUCA and the JMA-NHM, respectively.

Figure 6 shows the analytic solution and the simulation results from ASUCA and the JMA-NHM. Note that the effect of Rayleigh damping does not appear in Fig. 6 as the displayed domain is lower 12 km of the computational domain. The difference between the mountain wave simulated by ASUCA and the related analytical solution is smaller than that of the JMA-NHM. The normalized L2 norm of the error in the vertical velocity from the analytic solution for ASUCA and JMA-NHM results are 0.192 and 0.477, respectively. Note that the error in ASUCA is smaller than that in the JMA-NHM even though the time-step interval used in ASUCA is three times larger in this experiment.

Fig. 6

b. Rising thermal simulation

Numerical simulation for a rising thermal in a uniform horizontal flow in a two-dimensional adiabatic atmosphere, based on Wicker and Skamarock(1998), was carried out to evaluate basic performance for idealized convection and advection. The grid spacing is 125 m in both the x- and z-directions, and the computational domain is 20 km wide and 10 km deep. The initial thermal (diameter: 4 km) is placed at a height of 2 km with a potential temperature of 2 K higher than the surrounding environment and neutral stratification. The test imposes a uniform horizontal flow of 20 ms^{-1} and integrated for 1000 s, so that the thermal is laterally advected in a horizontally periodic domain and should be located in the center of the horizontal domain. A time-step interval of 2 s is used for ASUCA, while a 1 s time interval is used for the JMA-NHM because serious deterioration in simulation is produced with a 2 s interval. Fig. 7

Figure 7 shows the results for ASUCA and the JMA-NHM. The potential temperature and vertical velocity fields with ASUCA are symmetrical, while the potential temperature field with the JMA-NHM is much less symmetrical and the vertical velocity field is distorted and dispersive. The asymmetric result produced by JMA-NHM is mainly due to its fourth-order advection and leapfrog time integration scheme, as shown by Wicker and Skamarock(1998). The normalized L2 norm of the error in the vertical velocity, using the results from each model simulation with no horizontal flow as the benchmark, are 0.189 for ASUCA and 0.236 for JMA-NHM, respectively.

6.2 Performance as an operational NWP

This section compares the performance of the ASUCA-LFM (the 2 km-resolution operational regional model) to that of the NHM-LFM (Aranami et al. 2015).

A simulation involving Karman vortex streets, which often form downwind of islands during the cold-air outbreaks in winter, is presented here as an example of favorable representation using ASUCA dynamics. In Fig. 8, the ASUCA-LFM appears to reproduce the phenomenon better than the NHM-LFM. The JMA-NHM with numerical diffusion coefficients weaker than those of operational configuration could reproduce the Karman vortexes streets. However, these weakened values frequently cause computational instability. Fig. 8

In regional models, the predicted synoptic-scale pressure field should be consistent with that prescribed as the lateral boundary condition. Figure 9 shows differences in sea level pressure forecasts between the LFM and the external model (MSM) providing the boundary condition for 1200 UTC on 25 Dec. 2012. The ASUCA-LFM (left) follows MSM prediction at the synoptic-scale, while the local pattern differs due to differences in their prediction properties. However, the synoptic-scale pressure field determined from the NHM-LFM (right) deviates from the prediction of the MSM. This superior consistency mainly comes from improved total mass conservation in the ASUCA-LFM. The lateral boundaries control the net mass flux of the model domain, and consequently control the synoptic-scale pressure field. ASUCA explicitly calculates mass inflow and outflow because density is directly integrated as a prognostic variable. Accordingly, mass change across the entire domain coincides exactly with the total mass change due to inflow and outflow imposed at the region boundaries, source and sink at the surface, and density change by Rayleigh damping. However, the NHM-LFM, in which pressure is a prognostic variable, does not readily conserve total mass because errors are inevitable in evaluating density from the equation of state. Fig. 9

The ASUCA-LFM also achieved higher NWP performance including quantitative precipitation forecast (QPF) accuracy than NHM-LFM (Fig. 10). It should be noted that the QPF change is attributed to the updates of physical process schemes as well as the dynamical core itself. As it was also confirmed that ASUCA-LFM had better performance in terms of consistency with ground-based and radiosonde observations, ASUCA replaced JMA-NHM as the LFM in 2015, and the MSM in 2017 subsequently. Fig. 10

7. Future Plans

As described in Section 1, development of the new non-hydrostatic numerical model ASUCA was begun in 2007. The model is designed to ensure accuracy for NWP model, maintainability of components including physical processes and the data assimilation system and code structure suitable for future supercomputer architectures toward the establishment of a long-term operational forecasting infrastructure with a new-generation NWP model. ASUCA replaced the previous regional NWP model JMA-NHM (Saito et al. 2006), in 2015 as the LFM with 2 km resolution and in 2017 as the MSM with 5 km resolution. The ASUCA-based Mesoscale Ensemble Prediction System (Ono et al. 2021) has been in operation since 2019 and the ASUCA-based 4D-Var system (Ikuta et al. 2021), which is an outcome of relational developments, has been used to provide initial MSM fields since 2020. We close this paper with some ongoing development of ASUCA.

Increases of computational power in the future enable us to operate a regional NWP with higher model resolution and a wider forecast region, which could contribute to improving forecasts of severe weather. However, this may also give rise to new issues to be addressed in the improvement of high-resolution model accuracy.

While numerical models start to partly resolve cumulus convection with increased resolution, unresolved motions still remain to be parameterized due to the incompleteness of the motions resolved in the model. As assumptions made in conventional parameterization schemes are also often violated in such a regime, new parameterization schemes suitable for partially unresolved processes are required. This is known as the *gray zone* problem, and has recently drawn attention in the fields of research on cumulus convection (e.g., Arakawa and Wu 2013) and boundary layer turbulence (Honnert et al. 2020). It should be emphasized that the improvement of dynamical processes is even more important than ever in the gray zone as resolved part, which is represented by dynamical processes, increases at higher resolution.

The utilization of Koren's flux limiter enables the elimination of an explicit numerical filter and only advection scheme involves diffusion which highly depends on wind speed and direction (i.e. acting only in the windward direction). This results in overly frequent prediction of intense vertical velocity because diffusion relating to horizontal advection is relatively small in such situations. Accordingly, parameterization of horizontal diffusion with physical consideration may be necessary.

Some recent convection schemes (e.g., Kuell et al. 2007; Malardel and Bechtold 2019) relax the conventional assumption that the change of density by convection is negligible (i.e., environmental subsidence cancels the convective mass fluxes). The coupling of such physics schemes with the current dynamical core is a significant challenge because terms evaluated by those schemes relate to sound waves and their implementation may require the modification of the HE-VI scheme.

A numerical model with higher spatial resolution can also resolve smaller scales of topography, whose favorable representation is known to help improve model performance (Kanehama et al. 2019; Sandu et al. 2019). For instance, local circulation and precipitation processes derived from the topography can be more accurate. However, finer topographical representations incorporating steep slopes can significantly distort the shape of the control volume and affect numerical stability because the vertical axis in the terrain-following coordinate is restricted to the direction of gravity in the current configuration.

Steeper terrain can also cause significant pressure gradient force errors. In slope-containing grids, evaluation of horizontal pressure gradient force requires consideration of the vertical pressure gradient in generalized coordinates as per Eqs. (10) and (11). As the centered difference is used for the vertical pressure gradient, pressure is linearly interpolated using surrounding pressure values. Linear vertical interpolation of pressure creates larger discretization errors for steeper slopes because pressure changes with height are almost exponential. Modification of pressure gradient force computation via the interpolation of pressure to a constant height for adjacent columns (e.g., Klemp 2011) may reduce such errors. However, this requires further consideration in future work.

The currently operational non-hydrostatic model ASUCA has improved NWP accuracy for heavy rain and typhoons as well as contributing to a better understanding of extreme weather conditions around Japan and Asia. Ongoing development of the model is expected to improve NWP accuracy even more.

A. List of symbols

Symbols used in this paper are listed below in alphabetical order. The subscript α refers to dry air, water vapor, cloud water, cloud ice, rain, snow, and graupel for d, v, c, i, r, s and g respectively. Cartesian coordinates and generalized coordinates are referred to as (x, y, z) and (ξ, η, ζ), respectively.

A	momentum flux adjustment
β	parameter for determining sedimentation short time step
C	Courant number
C_{sed}	Courant number for sedimentation
C_p	specific heat capacity of dry air at constant pressure
C_v	specific heat capacity of dry air at constant volume
d_h	arbitrary parameter for determination of damping zone width from lateral boundaries
d_v	arbitrary parameter for determination of damping layer thickness from upper boundary
d_x	x-direction distance from lateral boundaries

d_y	y-direction distance from lateral boundaries
d_z	z-direction distance from upper boundary
D_x	x-direction size of computational domain
D_y	y-direction size of computational domain
ϵ	ratio of gas constants for dry air and water vapor (R_d/R_v)
f	Coriolis parameter
$\mathcal{F}$	fluxes of prognostic variables
F_M	mass flux from lateral boundaries
$F_{M,g}$	mass flux interpolated temporally from lateral boundaries
F_ρ	source, sink, and sub-grid transport term of total mass density
$F_{\rho\alpha}$	source, sink, and sub-grid transport term of density of α
$F_{\rho\theta_m}$	source, sink, and sub-grid transport term of $\rho\theta_m$
$F_{\rho u}$	source, sink, and sub-grid transport term of momentum for x-direction
$F_{\rho v}$	source, sink, and sub-grid transport term of momentum for y-direction
$F_{\rho w}$	source, sink, and sub-grid transport term of momentum for z-direction
$\mathfrak{g}$	gravity acceleration
γ	ratio of specific heat capacities for dry air at constant pressure and volume (C_p/C_v)
γ_h	arbitrary parameter for determination of damping strength at lateral boundaries
γ_v	arbitrary parameter for determination of damping strength at upper boundary
Γ	curvature of map factors
J	Jacobian of coordinate transformation from Cartesian to generalized coordinates

m	location-based function for determination of damping strength at lateral and/or upper boundarie
m_x	damping strength at x-direction lateral boundaries
m_y	damping strength at y-direction lateral boundaries
m_z	damping strength at upper boundary
m_1	map factor for x-direction
m_2	map factor for y-direction
nx	grid points number in x-direction
ny	grid points number in y-direction
ω	w-direction momentum at short time step
p	pressure
p_0	reference pressure
ϕ	scalar variable
Φ	flux limiter function
π	Exner function
q_α	density ratio of water substance α for total mass density
Q_θ	diabatic heating by physical processes
ρ	total mass density
ρ_α	density of category α
ρ_b	total density of dry air and water substances assumed to have zero terminal velocity
R_d	gas constant for dry air
R_v	gas constant for water vapor

$\mathfrak{R}$	term defined in Eq. (35)
$\mathfrak{R}_{\theta_m}$	term defined in Eq. (30)
$\mathfrak{R}_\rho$	term defined in Eq. (30)
$\mathfrak{R}_u$	x-direction momentum tendency terms solved with long time step
$\mathfrak{R}_v$	y-direction momentum tendency terms solved with long time step
$\mathfrak{R}_w$	w-direction momentum tendency terms solved with long time step
s	smoothness parameter for determination of flux limiter value
t	time
Δt	full model time step
τ	time at Runge-Kutta step
$\Delta\tau$	short time step for determination of acoustic and gravity wave modes
$\Delta\tau_{\mathrm{sed}}$	time-split step for sedimentation
θ	potential temperature
θ_m	modified moist potential temperature
u	velocity component in x-direction
U	velocity component in ξ-direction
v	velocity component in y-direction
V	velocity component in η-direction
w	velocity component in z-direction
W	velocity component in ζ-direction
W_{t_α}	terminal fall velocity of water substance α

z_s	surface height
z_T	model top height

Subscripts and superscripts

$()_x$	partial differential of () with respect to x
$()_y$	partial differential of () with respect to y
$()_z$	partial differential of () with respect to z
$\overline{()}$	basic state satisfying hydrostatic equilibrium
$()'$	deviation from basic state
$()^t$	value at time step
$()^\tau$	values at Runge-Kutta steps
$()^{\tau+\Delta\tau}$	values at HE-VI short time steps
$\widetilde{()}$	generalized coordinate momentum in HE-VI short time steps

B. Map projection and vertical coordinates in the operational models

The details of map projection and the vertical coordinates employed in the LFM and MSM, which are operational regional NWP with 2 km and 5 km resolutions respectively, are presented here.

ASUCA employs the Lambert conformal map projection. The map factors m_1 and m_2 (for the x and y directions) here are given by

$$m_1 = m_2 = m = \left(\frac{\cos\varphi}{\cos\varphi_1}\right)^{a-1}\left(\frac{1+\sin\varphi_1}{1+\sin\varphi}\right)^{a}, \tag{58}$$

$$a = \ln\left(\frac{\cos\varphi_1}{\cos\varphi_2}\right) \Bigg/ \ln\left\{\frac{\tan\left(\frac{\pi}{4}-\frac{\varphi_1}{2}\right)}{\tan\left(\frac{\pi}{4}-\frac{\varphi_2}{2}\right)}\right\}. \tag{59}$$

where φ is latitude, and $\varphi_1 = 30^\circ$ and $\varphi_2 = 60^\circ$ are used as standard parallels in the operational models.

The hybrid terrain-following vertical coordinate (Ishida 2007) is adopted to reduce the influences of topography with height. Since the horizontal pressure gradient term and the horizontal advection term are split into horizontal and vertical derivatives with non-flat coordinates, and the vertical grid spacing of NWP models is generally larger in the upper atmosphere, reduction of errors associated with related difference calculation is advantageous. The vertical coordinate ζ is transformed using

$$z = \zeta + z_s h\left(\zeta\right), \tag{60}$$

where z is height above sea level and z_s is ground height. The function $h\left(\zeta\right)$ is given by

$$h(\zeta) = \frac{b\left\{1 - \left(\dfrac{\zeta}{z_T}\right)^n\right\}}{b + \left(\dfrac{\zeta}{z_T}\right)^n}, \quad b = \frac{\left(\dfrac{z_c}{z_T}\right)^n}{1 - 2\left(\dfrac{z_c}{z_T}\right)^n}, \tag{61}$$

where z_T is the model top. z_c and n are parameters characterizing the influence of terrain; z_c is the height at which the center of the transition, between the terrain-following coordinate and the flat coordinate, is located, and n determines the varying rate of the transition. $z_c = 7000$m and $n = 3$ are employed in the LFM and MSM. Figure 11 shows the model levels over idealized mountain in the hybrid terrain-following coordinate in contrast to the basic terrain-following coordinate (Gal-Chen and Somerville 1975). The hybrid terrain-following coordinate is identical to the terrain-following and flat coordinate at $z = z_s$ and $z = z_T$, respectively, and the two coordinates are smoothly connected. Fig. 11

C. CFL condition for the advection with the Koren flux limiter and RK3 scheme

The one-dimensional advection equation with a uniform velocity $u(> 0)$ is considered as follows:

$$\frac{\partial \tilde{f}}{\partial t} = -u\frac{\partial \tilde{f}}{\partial x}, \quad x \in [0, 2\pi]. \tag{62}$$

The spatial direction is discretized with the grid spacing $\Delta x = 2\pi/N$ (N: the number of grid cells). We assume the following solution in Eq. (62):

$$\tilde{f}(x,t) = f(t)e^{ikx}, \quad k = 0, 1, \cdots, N/2. \tag{63}$$

The advection term is approximated by the first- or third-order upwind difference in the Koren flux limiter. The spatial derivative at the j-th grid using Eq. (63) is represented as

$$\left.\frac{\partial \tilde{f}}{\partial x}\right|_j \simeq \frac{\tilde{f}_j - \tilde{f}_{j-1}}{\Delta x} = \frac{1 - e^{-ik\Delta x}}{\Delta x}\tilde{f}_j, \tag{64}$$

for the first-order upwind difference. Substituting Eq. (64) into (62) yields

$$\frac{df}{dt} = \frac{u}{\Delta x}(e^{-ik\Delta x} - 1)f. \tag{65}$$

In the third-order Runge-Kutta time integration, Eq. (65) is stable if

$$|f^{n+1}/f^n| = |1 + z + z^2/2 + z^3/6| \leq 1, \quad z = C_1(e^{-ik\Delta x} - 1), \tag{66}$$

is satisfied for $0 \leq k\Delta x \leq \pi$. Here, the superscript n denotes the n-th timestep and $C_1 = u\Delta t/\Delta x$ is the Courant number. Solving Eq. (66) numerically, we can obtain the CFL condition $C_1 \leq 1.25$ for the first-order upwind difference.

The spatial derivative for the third-order upwind difference is written as

$$\left.\frac{\partial \tilde{f}}{\partial x}\right|_j \simeq \frac{2\tilde{f}_{j+1} + 3\tilde{f}_j - 6\tilde{f}_{j-1} + \tilde{f}_{j-2}}{6\Delta x} = \frac{2e^{ik\Delta x} + 3 - 6e^{-ik\Delta x} + e^{-2ik\Delta x}}{6\Delta x}\tilde{f}_j. \tag{67}$$

The CFL condition $C_1 \leq 1.61$ for the third-order upwind difference can be obtained by the similar procedure. This value coincides with that by Wicker and Skamarock(2002). Because the critical value of C_1 for the first-order is smaller than that for the third-order, $C_1 \leq 1.25$ should be chosen as the CFL condition for the Koren flux limiter.

Acknowledgements

We gratefully acknowledge all the colleagues developing ASUCA. We are also grateful to Dr. Nigel Wood and one anonymous reviewer who gave their constructive comments to help us improve quality of our manuscript.

Data Availability Statement

Some of the datasets and program codes used in this study are not publicly available due to the management policy of the Japan Meteorological Agency, but may be available from the relevant authors for reasonable usage upon request. All rights remain with JMA.

References

Arakawa, A., and V. R. Lamb, 1977: Computational design of the basic dynamical processes of the UCLA general circulation model. *Methods in Computational Physics*, Volume 17, Academic Press, 173–265.

Arakawa, A., and C.-M. Wu, 2013: A unified representation of deep moist convection in numerical modeling of the atmosphere. Part I. *J. Atmos. Sci*, **70(7)**, 1977–1992.

Aranami, K., T. Hara, Y. Ikuta, K. Kawano, K. Matsubayashi, H. Kusabiraki, T. Ito, T. Egawa, K. Yamashita, Y. Ota, Y. ishikawa, T. Fujita, and J. Ishida, 2015: A new operational regional model for convection-permitting numerical weather prediction at JMA. *CAS/JSC WGNE, Res. Activ. Atmos. Oceanic Modell.*, **45**, 0505–0506.

Aranami, K., and J. Ishida, 2004: Implementation of two dimensional decomposition for JMA non-hydrostatic model. *CAS/JSC WGNE, Res. Activ. Atmos. Oceanic Modell.*, **34**, 0301–0302.

Beljaars, A. C. M., and A. A. M. Holtslag, 1991: Flux parameterization over land surfaces for atmospheric models. *J. Appl. Meteor.*, **30**, 327–341.

Cats, G., V. T. Vu, and L. Wolters, 2008: Overlapping communications with calculations. *Hirlam newsletter*, **54**, 189–201.

Coakley, J. A., R. D. Cess, and F. B. Yurevich, 1983: The effect of tropospheric aerosols on the Earth's radiation budget: A parameterization for climate models. *J. Atmos. Sci*, **40(1)**, 116–138.

Dubal, M., N. Wood, and A. Staniforth, 2004: Analysis of parallel versus sequential splittings for time-stepping physical parameterizations. *Monthly Weather Review*, **132(1)**, 121–132.

Durran, D., 2010: *Numerical Methods for Fluid Dynamics: With Applications to Geophysics*. Texts in Applied Mathematics. Springer New York.

Gal-Chen, T., and R. C. J. Somerville, 1975: On the use of a coordinate transformation for the solution of the Navier-Stokes equations. *J. Comp. Phys.*, **17**, 209–228.

Gassmann, A., and H.-J. Herzog, 2007: A consistent time-split numerical scheme applied to the nonhydrostatic compressible equations. *Monthly Weather Review*, **135(1)**, 20–36.

Godunov, S. K., 1959: A difference method for numerical calculation of discontinuous solutions of the equations of hydrodynamics. *Mat. Sb. (N.S.)*, **47(89)**, 271–306.

Gryanik, V. M., C. Lüpkes, A. Grachev, and D. Sidorenko, 2020: New modified and extended stability functions for the stable boundary layer based on SHEBA and parametrizations of bulk transfer coefficients for climate models. *J. Atmos. Sci*, **77**, 2687–2716.

Gunn, R., and G. D. Kinzer, 1949: The terminal velocity of fall for water droplets in stagnant air. *J. Meteor.*, **6(4)**, 243–248.

Hara, T., K. Kawano, K. Aranami, Y. Kitamura, M. Sakamoto, H. Kusabiraki, C. Muroi, and J. Ishida, 2012: Development of physics library and its application to ASUCA. *CAS/JSC WGNE, Res. Activ. Atmos. Oceanic Modell.*, **42**, 0505–0506.

Honnert, R., G. A. Efstathiou, R. J. Beare, J. Ito, A. Lock, R. Neggers, R. S. Plant, H. H. Shin, L. Tomassini, and B. Zhou, 2020: The atmospheric boundary layer and the "Gray Zone" of turbulence: A critical review. *J. Geophys. Res.: Atmos.*, **125(13)**, e2019JD030317.

Ikawa, M., and K. Saito, 1991: *Description of a nonhydrostatic model developed at the Forecast Research Department of the MRI*, Volume 28. Tech. Rep. Meteor. Res. Inst. 238 pp.

Ikuta, Y., T. Fujita, Y. Ota, and Y. Honda, 2021: Variational data assimilation system for operational regional models at japan meteorological agency. *J. Meteor. Soc. Japan* in press.

Ishida, J., 2007: Development of a hybrid terrain-following vertical coordinate for JMA non-hydrostatic model. *CAS/JSC WGNE, Res. Activ. Atmos. Oceanic Modell.*, **37**, 0309–0310.

Ishida, J., C. Muroi, K. Kawano, and Y. Kitamura, 2010: Development of a new nonhydrostatic model "ASUCA" at JMA. *CAS/JSC WGNE, Res. Activ. Atmos. Oceanic Modell.*, **40**, 0511–0512.

JMA, 2014: ASUCA: Next generation non-hydrostatic model (in Japanese). *Separate volume of annual report of Numerical Prediction Division/Japan Meteorological Agency*, **60**. [Available at https://www.jma.go.jp/jma/kishou/books/nwpreport/60/No60_all.pdf.].

JMA, 2019a: Computer system. *Outline of The Operational Numerical Weather Prediction at The Japan Meteorological Agency* 1–8. [Available at https://www.jma.go.jp/jma/jma-eng/jma-center/nwp/outline2019-nwp/index.htm.].

JMA, 2019b: Numerical weather prediction models. *Outline of The Operational Numerical Weather Prediction at The Japan Meteorological Agency* 47–138. [Available at https://www.jma.go.jp/jma/jma-eng/jma-center/nwp/outline2019-nwp/index.htm.].

Joseph, J. H., W. J. Wiscombe, and J. A. Weinman, 1976: The delta-eddington approximation for radiative flux transfer. *J. Atmos. Sci*, **33**, 2452–2459.

Kain, J. S., 2004: The Kain-Fritsch convective parameterization: An update. *J. Appl. Meteor.*, **43**, 170–181.

Kain, J. S., and J. M. Fritsch, 1990: A one-dimensional entraining/detraining plume model and its application in convective parameterization. *J. Atmos. Sci.*, **47**, 2784–2802.

Kanehama, T., I. Sandu, A. Beljaars, A. van Niekerk, and F. Lott, 2019: Which orographic scales matter most for medium-range forecast skill in the northern hemisphere winter? *J. Adv. Model. Earth Syst.*, **11(12)**, 3893–3910.

Klemp, J. B., 2011: A terrain-following coordinate with smoothed coordinate surfaces. *Mon. Wea. Rev*, **139(7)**, 2163 – 2169.

Klemp, J. B., W. C. Skamarock, and J. Dudhia, 2007: Conservative split-explicit time integration methods for the compressible nonhydrostatic equations. *Mon. Wea. Rev*, **135(8)**, 2897–2913.

Koren, B., 1993: A robust upwind discretization method for advection, diffusion and source terms. *CWI Report NM-R9308.*

Kuell, V., A. Gassmann, and A. Bott, 2007: Towards a new hybrid cumulus parametrization scheme for use in non-hydrostatic weather prediction models. *Quart. J. Roy. Meteor. Soc*, **133(623)**, 479–490.

Lin, Y.-L., R. Farley, and H. Orville, 1983: Bulk parametarization of the snow field in a cloud model. *J. Climate Appl. Meteor.*, **22**, 1065–1092.

Lorenz, E. N., 1960: Energy and numerical weather prediction. *Tellus*, **12(4)**, 364–373.

Malardel, S., and P. Bechtold, 2019: The coupling of deep convection with the resolved flow via the divergence of mass flux in the IFS. *Quart. J. Roy. Meteor. Soc*, **145(722)**, 1832–1845.

Moncrieff, M. W., S. K. Krueger, D. Gregory, J.-L. Redelsperger, and W.-K. Tao, 1997: GEWEX cloud system study (GCSS) Working Group 4: Precipitating Convective Cloud Systems. *Bull. Amer. Meteor. Soc.*, **78(5)**, 831–846.

Nakanishi, M., and H. Niino, 2009: Development of an improved turbulence closure model for the atmospheric boundary layer. *J. Meteor. Soc. Japan*, **87**, 895–912.

Noilhan, J., and S. Planton, 1989: A simple parameterization of land surface processes for meteorological models. *Mon. Wea. Rev*, **117**, 536–549.

Ono, K., M. Kunii, and Y. Honda, 2021: The regional model-based mesoscale ensemble prediction system, MEPS, at the Japan Meteorological Agency. *Quart. J. Roy. Meteor. Soc*, **147(734)**, 465–484.

Saito, K., T. Fujita, Y. Yamada, J. Ishida, Y. Kumagai, K. Aranami, S. Ohmori, R. Nagasawa, S. Kumagai, C. Muroi, T. Kato, H. Eito, and Y. Yamazaki, 2006: The operational JMA nonhydrostatic mesoscale model. *Mon. Wea. Rev*, **134(4)**, 1266–1298.

Saito, K., T. Kato, H. Eito, and C. Muroi, 2001: *Documentation of the Meteorological Research Institute / Numerical Prediction Division Unified Nonhydrostatic Model*, Volume 42. Tech. Rep. Meteor. Res. Inst. 133 pp.

Samukawa, H., 2001: A parallel tridiagonal solver based on ETC ordering (in Japanese). *Trans. IPS. Japan*, **42(4)**, 779–787.

Sandu, I., A. van Niekerk, T. Shepherd, S. Vosper, A. Zadra, J. Bacmeister, A. Beljaars, A. Brown, A. Dörnbrack, N. McFarlane, F. Pithan, and G. Svensson, 2019: Impacts of orography on large-scale atmospheric circulation. *npj Climate Atmos. Sci.*, **2**, 10.

Skamarock, W. C., J. D. Doyle, P. Clark, and N. Wood, 2004: A standard test set for nonhydrostatic dynamical cores of NWP models.

In 16th Conference on Numerical Weather Prediction, Seattle WA, USA P2.17.

Skamarock, W. C., and J. B. Klemp, 1992: The stability of time-split numerical methods for the hydrostatic and the nonhydrostatic elastic equations. *Mon. Wea. Rev*, **120(9)**, 2109 – 2127.

Skamarock, W. C., and J. B. Klemp, 1994: Efficiency and accuracy of the Klemp-Wilhelmson time-splitting technique. *Mon. Wea. Rev*, **122(11)**, 2623–2630.

Straka, J. M., R. B. Wilhelmson, L. J. Wicker, J. R. Anderson, and K. K. Droegemeier, 1993: Numerical solutions of a non-linear density current: A benchmark solution and comparisons. *Int. J. Num. Meth. Fluids*, **17**, 1–22.

Sweby, P. K., 1984: High resolution schemes using flux limiters for hyperbolic conservation laws. *SIAM J. Numer. Anal.*, **21(5)**, 995–1011.

Wicker, L. J., and W. C. Skamarock, 1998: A time-splitting scheme for the elastic equations incorporating second-order Runge-Kutta time differencing. *Mon. Wea. Rev*, **126(7)**, 1992 – 1999.

Wicker, L. J., and W. C. Skamarock, 2002: Time-splitting methods for elastic models using forward time schemes. *Mon. Wea. Rev*, **130(8)**, 2088–2097.

Yabu, S., 2013: Development of longwave radiation scheme with consideration of scattering by clouds in JMA global model. *CAS/JSC WGNE, Res. Activ. Atmos. Oceanic Modell.*, **43**, 0407–0408.

List of Figures

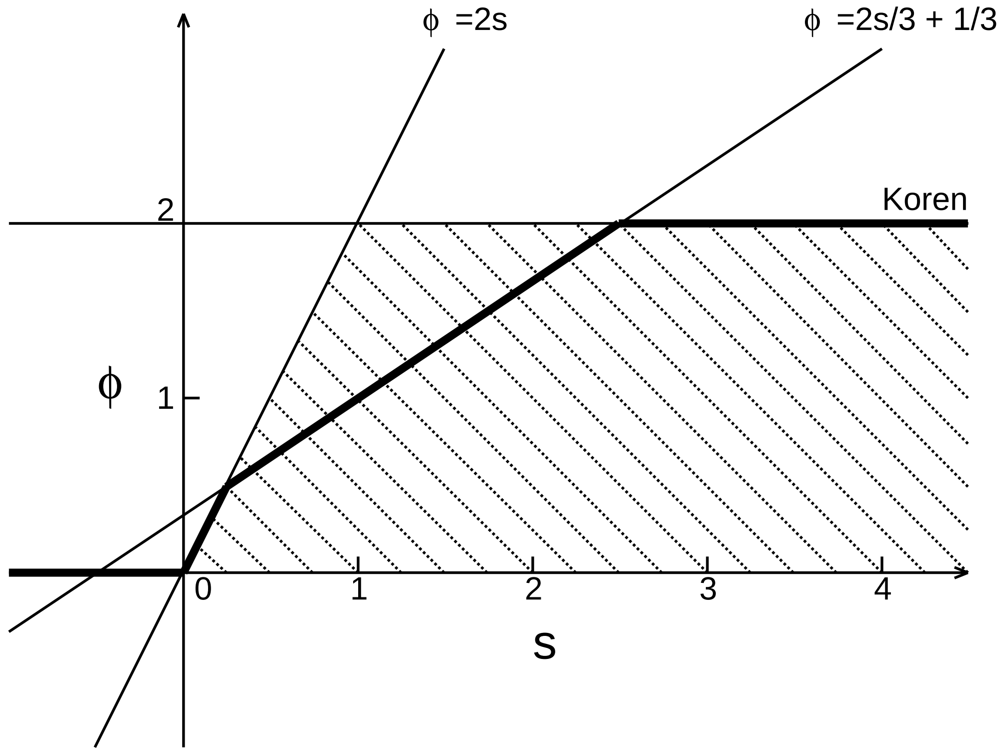

Fig. 1: Flux limiter function proposed by Koren (thick line). The horizontal and vertical axes represent the smoothness parameter s defined in Eq. (19), and the flux limiter function Φ, respectively. The function must lie within the shaded region for a monotonicity-preserving scheme.

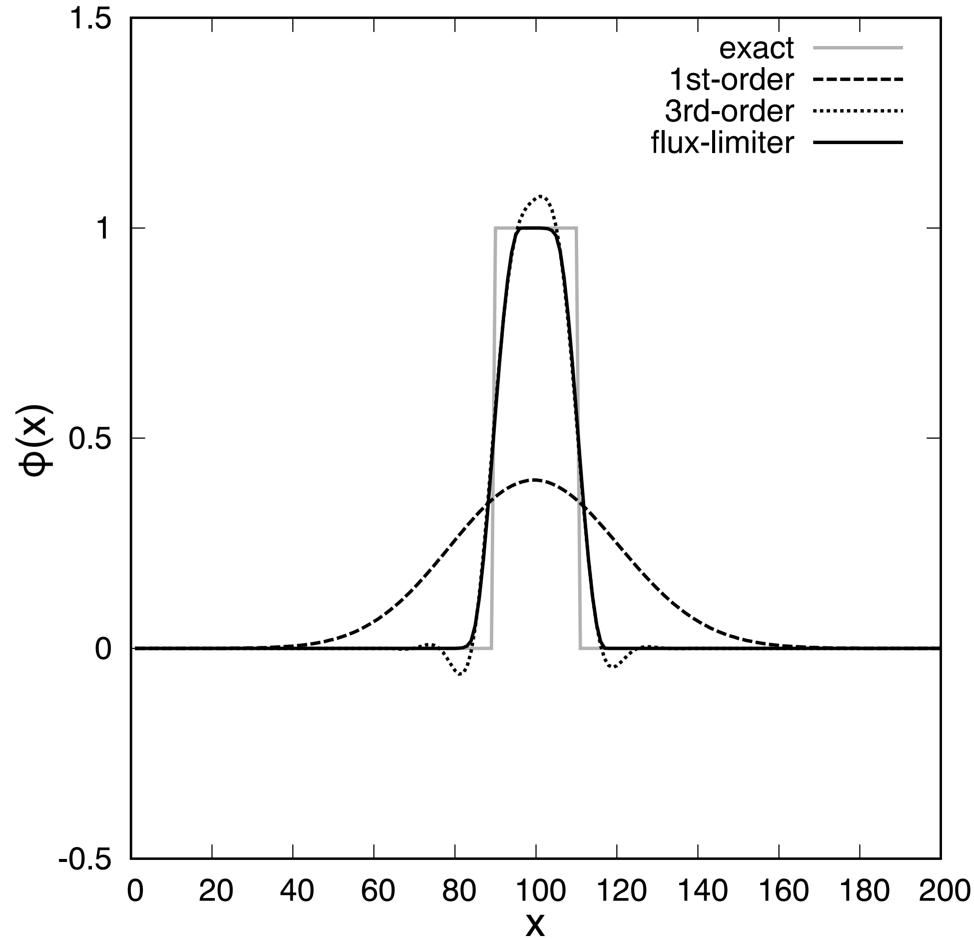

Fig. 2: Comparison of advection schemes for a one-dimensional transport problem shown in (18) with uniform velocity. The horizontal and vertical axes represent the position x and scalar variable ϕ, respectively. Solid gray, dashed, dotted and solid black lines indicate the exact solution, first order, third order and Koren's flux limiter schemes, respectively.

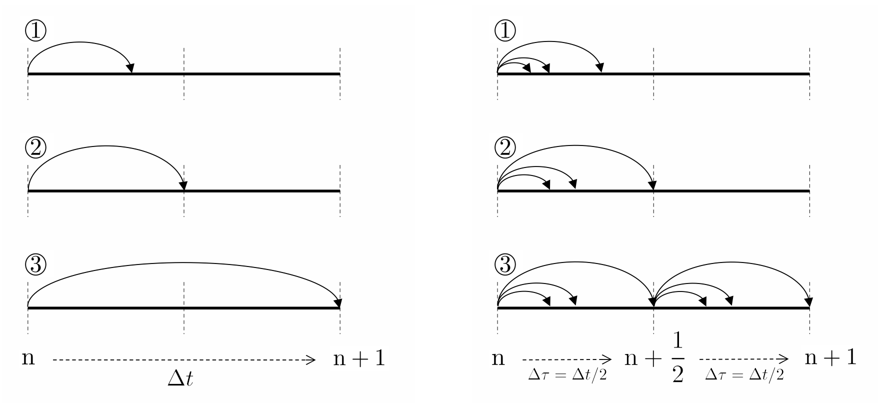

(a) original RK3 (b) RK3 with time splitting

Fig. 3: (a) Original RK3 scheme, and (b) RK3 with time splitting. Circled numbers correspond to each RK3 stage. The third stage is split into two sub-steps in (b).

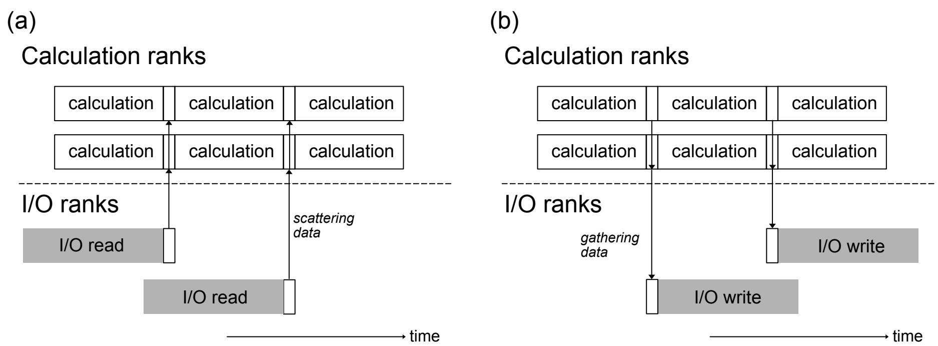

Fig. 4: Schematic diagram of I/O server approach for (a) reading data from disks and scattering data to calculation ranks and (b) gathering data from calculation ranks and writing data to disks. The computation and disk I/O are simultaneously executed in calculation and I/O ranks, respectively.

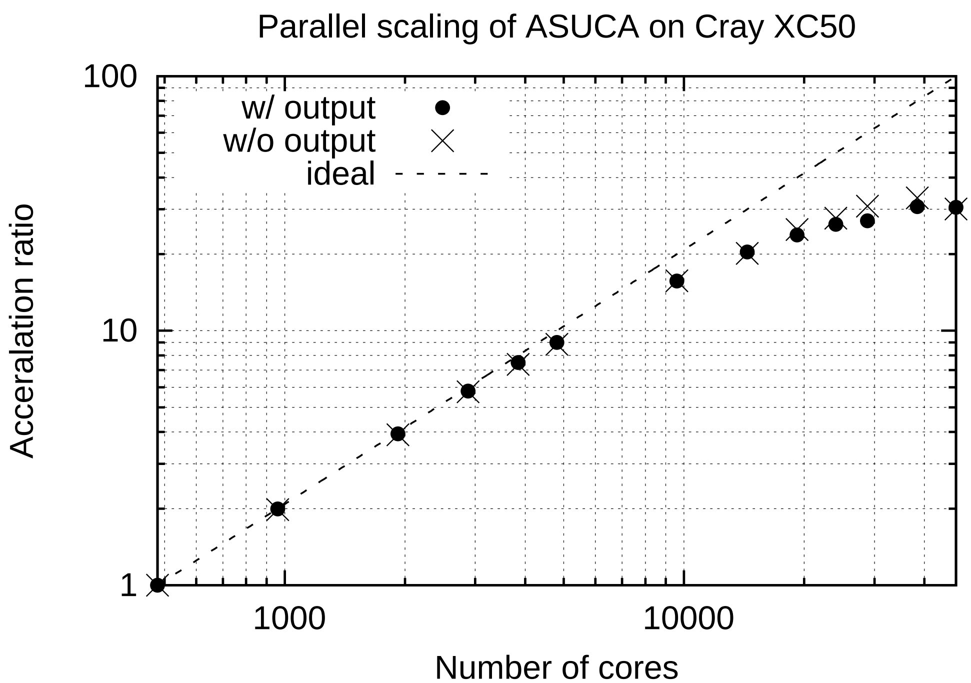

Fig. 5: Acceleration ratio determined with JMA's supercomputer system in operational LFM configuration. The dashed line shows the ideal acceleration ratio. The horizontal axis represents the number of CPU cores, and the vertical axis represents the acceleration ratio compared to speed with 480 cores.

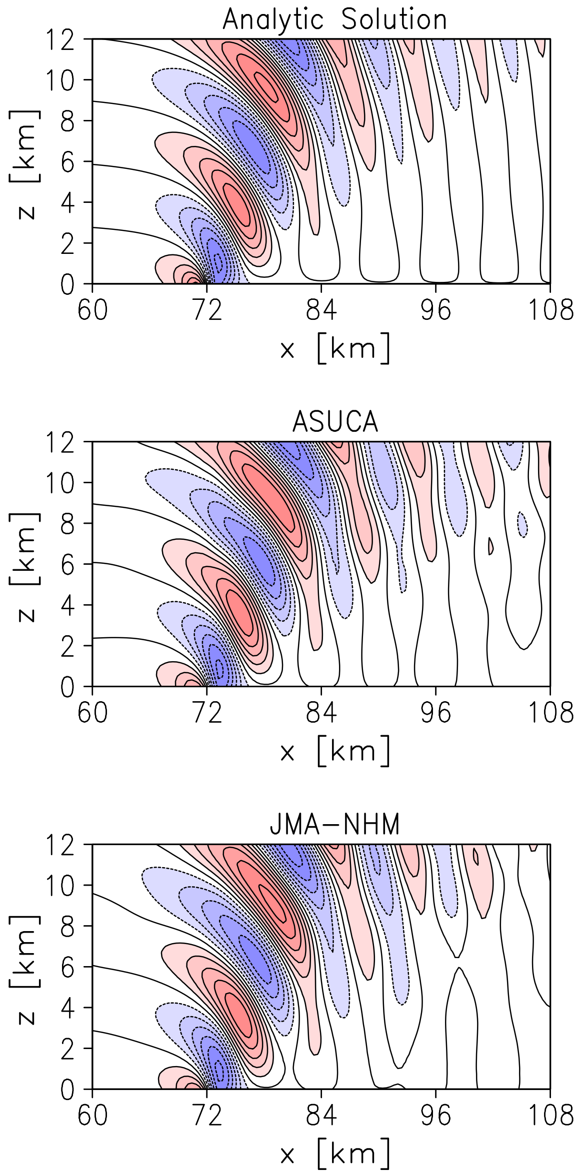

Fig. 6: Vertical velocity for mountain wave testing of (top) analytic solution, (middle) ASUCA simulation result after 9000 s, and (bottom) the JMA-NHM. Lower 12 km in vertical and 48 km (60 km-108km) in horizontal part of the computational domain is displayed. Contour interval is 6.0×10^{-4} m s^{-1}.

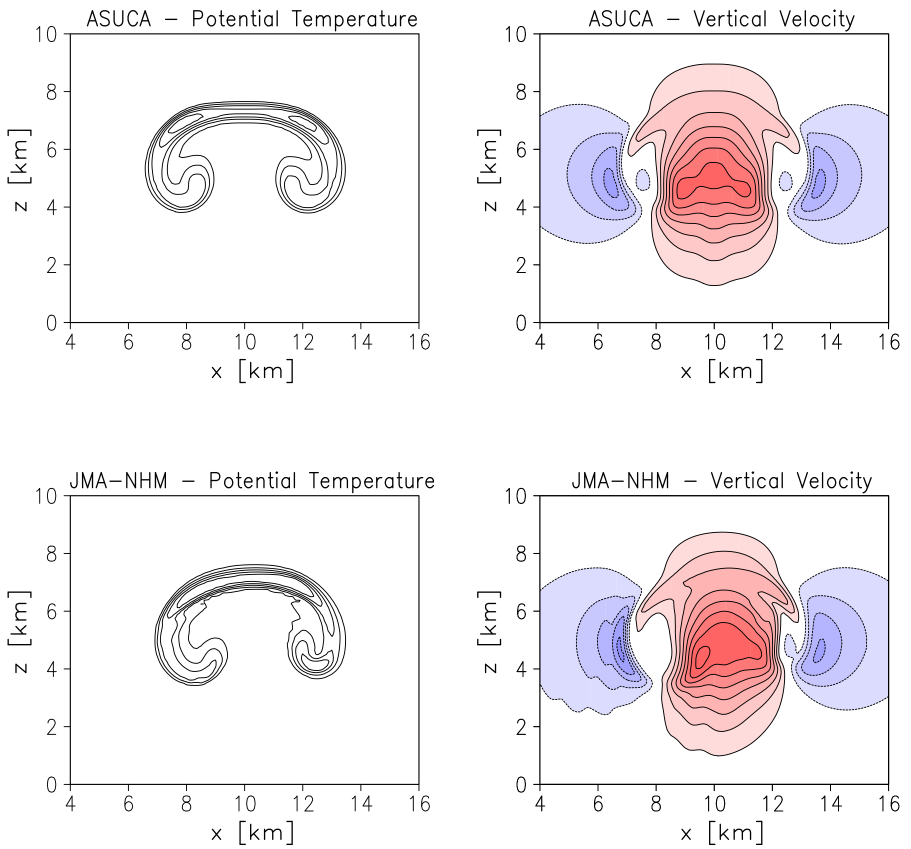

Fig. 7: Results for rising thermal in a uniform horizontal flow testing simulated using (top) ASUCA and (bottom) the JMA-NHM. The panels on the left and right show potential temperature (contour interval 0.25 K) and vertical velocity (contour interval 1.5 ms^{-1}), respectively.

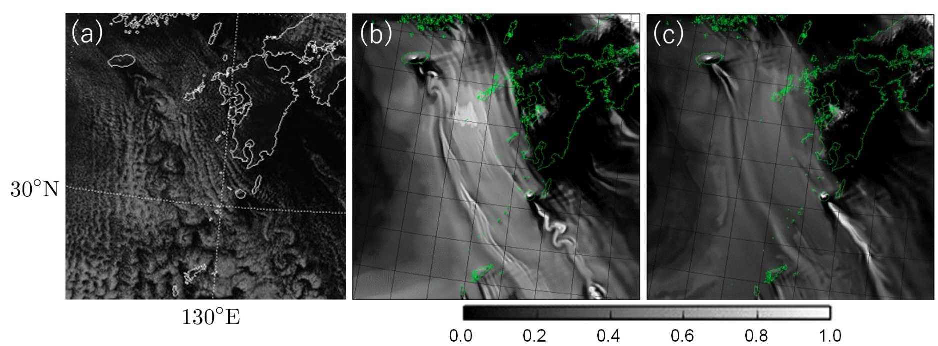

Fig. 8: (a) Visible satellite imagery from 0530 UTC on 9 Jan. 2015. Cloud fraction at low level simulated using (b) ASUCA-LFM and (c) NHM-LFM with a 5.5-hour lead time and an initial time of 0000 UTC on 9 Jan. 2015.

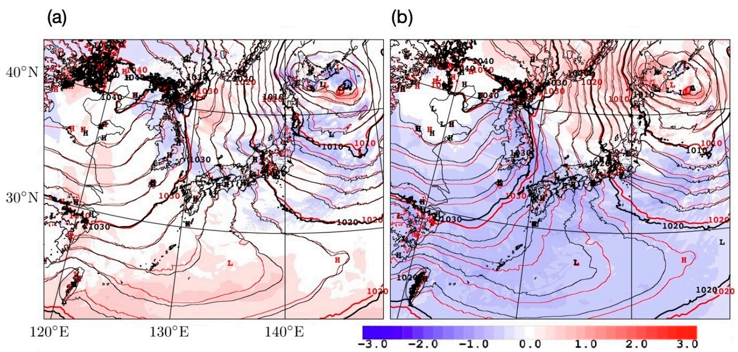

Fig. 9: Sea level pressure simulated using (a) ASUCA-LFM and (b) NHM-LFM. Black and red contours indicate sea level pressure [hPa] in the LFM with a 9-hour lead time and an initial time of 0300 UTC on 25 Dec. 2012 and the MSM with a 12-hour lead time and an initial time of 0000 UTC on 25 Dec. 2012, respectively. Shading represents sea level pressure differences between the LFM and the MSM.

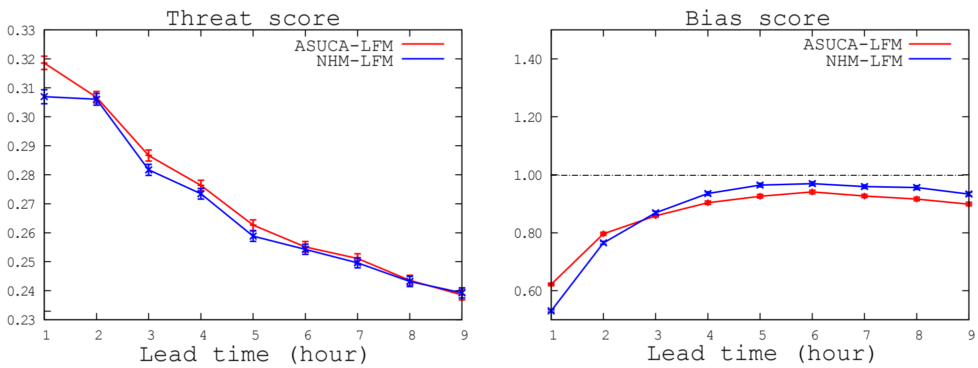

Fig. 10: The threat score (TS; left) and the bias score (BI; right) for 1 hour precipitation accumulation with ASUCA-LFM(red) and NHM-LFM (blue), for a threshold of 1 mm/hour. The forecasts are verified against the Radar/Rainguage-Analyzed Precipitation, which is operationally produced by JMA, for summer season in 2012. TS measures the fraction of observed and/or forecast events that were correctly forecasted, and the accuracy of forecasts is higher as TS approaches to the maximum value of unity. BI measures the frequency correspondence between forecast and observation events. If BI is larger (smaller) than unity, the frequency of events is over-estimated (underestimated).

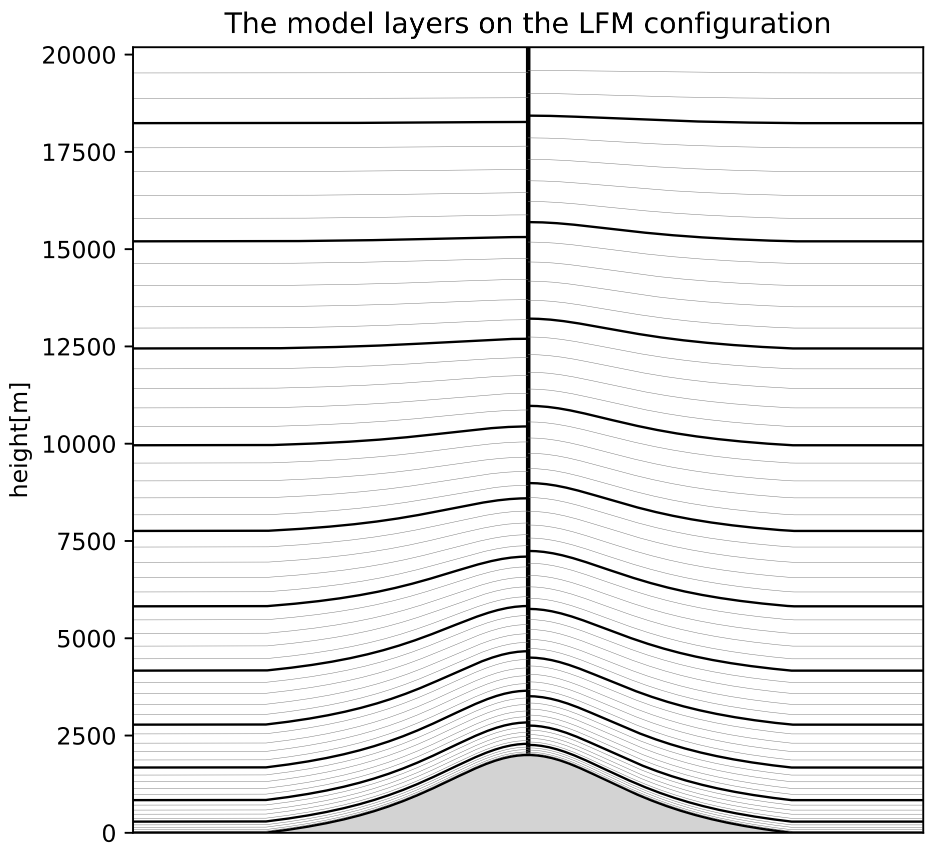

Fig. 11: The model vertical half-levels in the hybrid terrain-following (left) and classical terrain-following (right) coordinates over idealized mountain with the maximum height of 2000m. Every five layers are highlighted with thick lines. The LFM configuration is used for the coordinate parameters and the model top.

List of Tables

Table 1: Physical process schemes used in the LFM operated since March 2021.

Process	Scheme
Radiation	Short wave: two-stream with delta-Eddington approximation (evaluated every 15 minutes) (Joseph et al. 1976; Coakley et al. 1983) Long wave: two-stream absorption approximation (evaluated every 15 minutes) (Yabu 2013)
Boundary layer	Mellor-Yamada-Nakanishi-Niino Level-3 scheme (Nakanishi and Niino 2009)
Surface flux	Monin-Obukhov similarity theory with stability function (Beljaars and Holtslag 1991; Gryanik et al. 2020)
Soil	Ground temperature prediction using an eight-layer ground model (Noilhan and Planton 1989)
Convection	Kain-Fritsch convection scheme (Kain 2004; Kain and Fritsch 1990)
Cloud microphysics	Single moment, three-ice bulk method (Lin et al. 1983; Ikawa and Saito 1991)